Connectome simulations identify a central pattern generator circuit for fly walking

Sarah M. Pugliese[1,2,3], Grant M. Chou[3], Elliott T.T. Abe[2], Denis Turcu[4], Jackson K. Lancaster[2], John C. Tuthill[3,†], and Bingni W. Brunton[2,†]

[1]Neuroscience Graduate Program, University of Washington, Seattle, WA, USA
[2]Dept of Biology, University of Washington, Seattle, WA, USA
[3]Dept of Neurobiology & Biophysics, University of Washington, Seattle, WA, USA
[4]Allen Institute for Brain Science, Seattle, WA, USA
[†]Co-senior, corresponding authors: bbrunton@uw.edu, tuthill@uw.edu

Abstract

Animal locomotion relies on rhythmic body movements driven by central pattern generators (CPGs): neural circuits that produce oscillating output without oscillating input. However, the circuit structure of a CPG for walking is not known in any animal. To identify the cells and synapses that underlie rhythmic leg movement in walking flies, we developed dynamic simulations of the *Drosophila* ventral nerve cord (VNC) connectomes. We used a computational activation screen to identify descending neurons from the brain that drive rhythmic activity in leg motor neurons, including a command neuron for walking (DNg100). By synthetic pruning of the VNC network, we isolated a minimal three-neuron rhythm-generating circuit consisting of one inhibitory and two excitatory interneurons. A model of this core CPG circuit is sufficient to generate motor rhythms, and the two excitatory neurons are necessary in the VNC network model. Connectome simulations also predicted that parallel descending neurons (DNb08) produce rhythmic leg movements, which we experimentally confirmed using optogenetics in behaving flies. Our results reveal the cellular identity and synaptic structure of a putative CPG circuit for fly walking.

Most animals move through the world using rhythmic movements, such as undulation of the body to swim and slither, or cyclic movement of legs and wings to walk or fly. Early studies of vertebrate locomotion proposed that motor rhythms are generated by sensory feedback from proprioceptors, which reflexively trigger the next phase of the locomotor cycle [1]. However, subsequent work on cats [2], crayfish [3], and locusts [4] demonstrated that motor rhythms persisted even after transection of sensory nerves. These results suggested that the central nervous system can generate rhythmic activity patterns on its own, without proprioceptive feedback or other rhythmic inputs. Such rhythm-generating circuits became known as *central pattern generators* (CPGs). CPGs have been studied intensively in both vertebrates and invertebrates, where they are believed to be crucial in locomotor rhythms such as walking, flying, and swimming, and non-locomotor rhythms such as breathing, feeding, scratching, circulation, and singing [5, 6, 7].

Different CPG circuits are known to generate rhythms using many distinct mechanisms. For example, in the crustacean stomatogastric ganglion (STG, [8]) as well as the leech heart and swimming CPGs [9, 10], neurons possess specialized cellular properties that support rhythm generation, such as intrinsic bursting, plateau potentials, and post-inhibitory rebound. The preBötzinger complex, which controls breathing in vertebrates, contains neurons that intrinsically burst, even when isolated from the rest of the network [11]. However, specific patterns of synaptic connectivity between neurons, such as mutual inhibition, can also contribute to rhythm generation in these circuits [12]. For example, the swimming CPG of the nudibranch *Tritonia* is a network oscillator whose cells lack intrinsic bursting properties [13]. Overall, studies of diverse CPG circuits suggest that rhythm generation is often an emergent property of the network as a whole, rather than being reliant on one specific mechanism [14, 15].

Despite considerable evidence that CPGs produce the walking rhythm in vertebrates and invertebrates, the specific implementation of a CPG circuit for walking is not known for any animal [5, 7]. Lacking knowledge of the anatomy, connectivity, and electrophysiological properties of CPG neurons, most computational models for animal walking rely on the presence of intrinsic bursting neurons as components of balanced excitation-inhibition networks (e.g., [16, 17]), or abstract all neural mechanisms to replace the CPG circuit with an oscillator equation (e.g., the Kuramoto oscillator [18]). Much theoretical work has focused on how locomotor CPGs interact within and across limbs [19, 20, 21, 22] and with the body [23, 24, 25] to produce coordinated gaits, without explicitly modeling the underlying pattern-generating mechanisms.

Here, we seek to identify the cellular components of CPG circuits that underlie walking in the fruit fly *Drosophila* using a computational modeling approach enabled by comprehensive datasets of neural connectivity. Flies are agile and robust walkers, and the adult fly is the only limbed animal whose nervous system is almost completely mapped at synaptic resolution using electron microscopy reconstruction of cells and synapses (known as *connectomics*, [26, 27, 28, 29]). Recent connectome datasets of the fly ventral nerve cord (VNC, [27, 28]), which is analogous to the vertebrate spinal cord (**Fig. 1a**), provide a unique opportunity to identify the core cell types and synaptic connections that comprise fly CPGs. Beyond synaptic connectivity maps, published VNC connectome datasets have been extensively annotated [30, 31, 32] and include predictions of neurotransmitter identity and muscle targets of leg motor neurons.

Based on analyses of small nervous systems that have been mapped using connectomics (e.g., the *C. elegans* worm) and electrophysiology (e.g., the crustacean STG), it has been argued that computational models of neural dynamics are not sufficiently constrained by connectivity alone [33, 34]. Existing fly connectome datasets lack important biophysical and molecular parameters, such as the expression of ion channels, receptors, neuromodulators, and gap junctions. Despite these gaps, several recent studies have developed connectome-constrained simulations of circuits within the fly central brain. One study directly modeled neural activity using a spiking network with fixed parameters [35], while others have leveraged neural recording data to infer unknown parameters with machine learning [36, 37, 38]. Here, we used direct numerical simulation of the fly VNC connectomes to identify descending pathways from the brain that produce rhythmic leg movement during sustained activation and corroborated these predictions with optogenetics experiments in behaving flies. We then developed a computational pruning screen to isolate a minimal rhythm-generating circuit of three VNC interneurons that is sufficient to generate rhythmic leg motor activity. We propose that this three-neuron circuit constitutes the core CPG for fly walking.

Connectome simulations of motor activity from descending input

To identify rhythm-generating circuits for fly walking, we developed a firing rate model based on the connectivity of neurons controlling the front legs in the male adult nerve cord (MANC) dataset [27]. The full simulated network consisted of 4,604 neurons (**Fig. 1b**), including 1,318 descending neurons (DNs), 144 leg motor neurons, and 3,142 premotor neurons within the VNC, which we defined as all neurons that synapse onto motor neurons [30]. The 3,780,908 synapses among these neurons formed elements of a weight matrix $\mathbf{W}$, for which the entries w_{ij} are the synapse counts from presynaptic neuron j to postsynaptic neuron i (**Fig. 1b**). We used the predicted neurotransmitter identity of neuron j to assign positive or negative weights for excitatory (cholinergic) or inhibitory (GABAergic, glutamatergic) cells, respectively. We chose a rate model in part because some neurons in the insect VNC, including premotor neurons active during walking, are nonspiking [39, 40, 41, 42].

We modeled the firing rates of neurons in the network $r_i(t)$ as a system of ordinary differential equations, given their synaptic and exogenous inputs. Firing rates evolved according to

$$\tau_i \frac{dr_i}{dt} = \left[r_i^{\max} \tanh\left(\frac{a_i}{r_i^{\max}} \left(I_i(t) + b \sum_j w_{ij} r_j(t) - \theta_i \right) \right) \right]_+ - r_i(t). \tag{1}$$

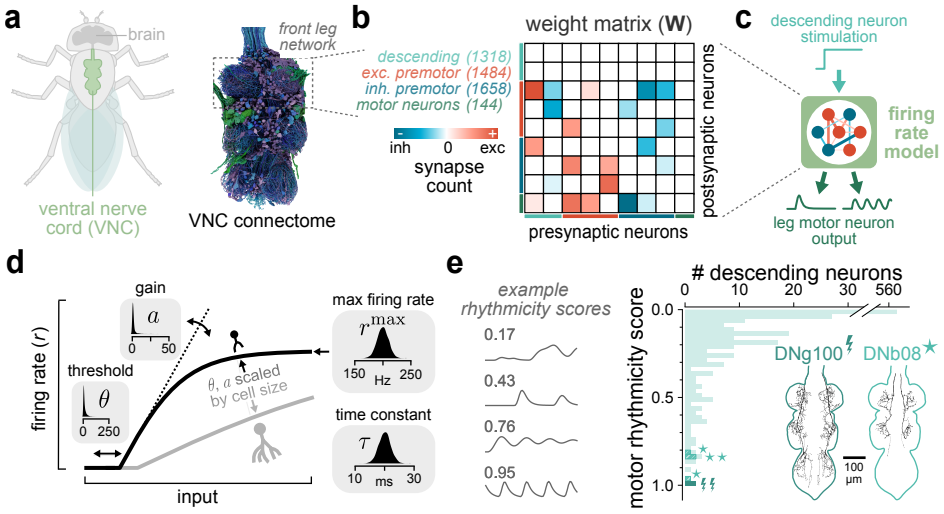

Figure 1: Direct numerical simulations of fly ventral nerve cord (VNC) connectomes identify descending pathways for rhythmic leg motor control. a, The *Drosophila* VNC, which is analogous to the vertebrate spinal cord. We constructed network models based on the connectivity of cells in the front leg neuropil from the male (MANC) and female (FANC) adult nerve cord connectomes (dashed box). **b**, Schematized synaptic weight matrix **W**. Labels at left indicate the number of neurons in the MANC network model. **c**, Schematic of model and descending neurons (DNs) activation screen. Each DN was stimulated with tonic input, then transformed by a firing rate model of the VNC connectome (**Equation 1**). We assessed the rhythmicity of leg motor neuron firing rates. **d**, Each neuron in the model had four biophysical parameters and a rectified tanh activation function. Insets show the distributions from which the parameters were drawn randomly at every simulation replicate. Gain a and threshold θ were scaled by the size of each neuron (see Methods). **e**, A computational screen of DNs identified cells that produce rhythmic activity in leg motor neurons. At left are example motor neuron activity traces and their rhythmicity scores. Each DN's score was an average of 16 replicates using different random parameter seeds. Two specific DN types are highlighted (DNb08 as stars, DNg100 as bolts, with their anatomy shown as insets).

The input to a given neuron i was a sum of firing rates $\{r_j(t)\}$ weighted by the synapse counts w_{ij}, and any exogenous input $I_i(t)$ to the neuron. A constant b scaled the synaptic inputs relative to the external input and had the same value for all neurons. This summed input was then passed through a nonlinearity, defined as a positive-rectified (indicated by $[\cdot]_+$) hyperbolic tangent, so that firing rates were non-negative and gradually saturated at a maximum value (**Fig. 1d**).

Each model neuron had four biophysical parameters: gain a_i, firing threshold θ_i, maximum firing rate $r_i^{\max}$, and time constant τ_i. We modeled these unmeasured cellular parameters as random samples from biophysically plausible distributions. In other words, we did not fine-tune any parameters, and instead simulated large numbers of computational replicates of each network (as was done in [43]), so that our overall results are generally interpretable without precise knowledge of the 18,416 biophysical parameters in the network. For each neuron i in each simulation, we drew its biophysical parameters from distributions based in part on published physiological measurements of fly neurons [44, 42]; values were also consistent with previous fly network models [45, 35]. We normalized the gain and threshold parameters to account for the fact that larger neurons have proportionally lower input resistance and are therefore less excitable [46]. Note that no neuron had intrinsic bursting or other longer-timescale membrane properties. Details on the construction and numerical implementation of simulations are elaborated in Methods.

We used our model to investigate descending control of rhythmic movement by conducting a computational activation screen of all 933 excitatory DNs (i.e., DNs predicted to release acetycholine). We activated each DN with a step input and evaluated the output of motor neurons innervating the front legs over 16 random simulation replicates. Only a small fraction of DNs produced highly rhythmic activity in leg motor neurons (**Fig. 1e**). To quantify the rhythmicity of simulated motor neuron activity, we developed a *motor rhythmicity score* that was calculated from the autocorrelations of all active motor neurons, averaged over

all replicates. The motor rhythmicity score was normalized between 0 and 1, where 0 is not rhythmic and 1 corresponds to perfectly periodic oscillations (see example traces in **Fig. 1e**). Out of the 933 DNs activated in simulation, 184 (19.7%) failed to produce interpretable network activity (as defined in Methods) in all replicates and could not be scored. Of the 749 remaining, 455 (60.7%, or 48.8% of the total) scored zero. Only 37 DNs (4.9%, 4.0% of total) had an average score greater than 0.5 (**Supplementary Table 1**). Activation screen results were qualitatively similar for the left and right front legs. In subsequent analyses, we focus on two descending neuron types, DNg100 and DNb08, because every DN of these two types produced among the highest rhythmicity scores.

DNg100 activation drives rhythmic leg motor neuron activity and controls stepping frequency

DNg100 is among the only cell types known in flies to function as descending command neurons for walking; a recent study found that optogenetically stimulating DNg100 neurons initiated forward walking, even in headless flies ([47], where DNg100 is referred to as BDN2). To further investigate the impact of DNg100 activation in the VNC, we constructed simulations from two independent connectome datasets and found that DNg100 activation consistently produced leg motor rhythms **Fig. 2a–d**. Specifically, we simulated activation of the left DNg100 using the male (MANC, [27]) and female (FANC, [28]) adult nerve cord networks, repeating 1024 replicates for each network, each with randomly drawn biophysical parameters. In both networks, DNg100 reliably drove rhythmic activity in several front leg motor neurons (**Fig. 2a–d**). Motor rhythmicity scores were comparable for FANC and MANC simulations, but more leg motor neurons were recruited in the FANC network (**Fig. 2c–d**). These results suggest that the VNC network downstream of DNg100 contains a CPG circuit.

To determine the extent to which leg motor rhythms depend on the precise synaptic weights mapped in the connectomes, we repeated DNg100 activation after systematically adding noise to the weight matrix. In particular, we perturbed $\mathbf{W}$ from the MANC dataset by adding noise η_{ij} to each entry w_{ij}. The magnitude of perturbations η_{ij} was drawn from a normal distribution with standard deviation proportional to w_{ij} (so that $\eta_{ij} \sim \mathcal{N}(0, \sigma w_{ij})$, where σ varied from 0 to 50%). Perturbed weights were truncated so that w_{ij} could not change signs. In this way, perturbations preserved the structure of the connectivity matrix: no new connections were added and no synapses changed sign. We found that motor rhythms were robust up to 10% added noise (**Fig. 2e**). This value is close to the estimated uncertainty of the synapse counts in connectome datasets, which reflects both real biological variability and computational errors in automated synapse detection [26, 48]. These results suggest that motor rhythms generated by DNg100 arise from the general structure of the connectivity matrix, rather than the precise synapse counts.

During walking, motor neurons are active with specific phase relationships among legs and between antagonistic muscles. However, in flies, it remains unclear whether such coordination patterns are produced centrally by feedforward mechanisms (e.g., CPGs) or require sensory feedback. By simulating bilateral activation of DNg100 cells, we found that feedforward circuits downstream of DNg100 produced a consistent phase offset between antagonistic muscles (coxa promotor and remotor) within the left leg (**Fig. 2f**). Although the left and right leg motor neurons both had rhythmic activity, there was not a consistent phase relationship between the two sides. In other words, our simulations produced signatures of motor coordination within each leg, but descending drive alone was insufficient to produce realistic inter-leg coordination.

Another unexpected result of our DNg100 simulations was that the oscillations produced in leg motor neurons roughly matched the stepping frequency of real walking flies (∼7–15 Hz, [49, 50]). In our model, oscillation frequencies were determined by the range of time constant parameters τ (**Supplementary Fig. 1**, see also Methods for a mathematical relationship between frequency and τ in the linearized system). Exploring other simulation parameters, we noticed that increasing the magnitude of DNg100 stimulation increased the frequency of motor neuron oscillations (**Fig. 2g**). Previous work had shown

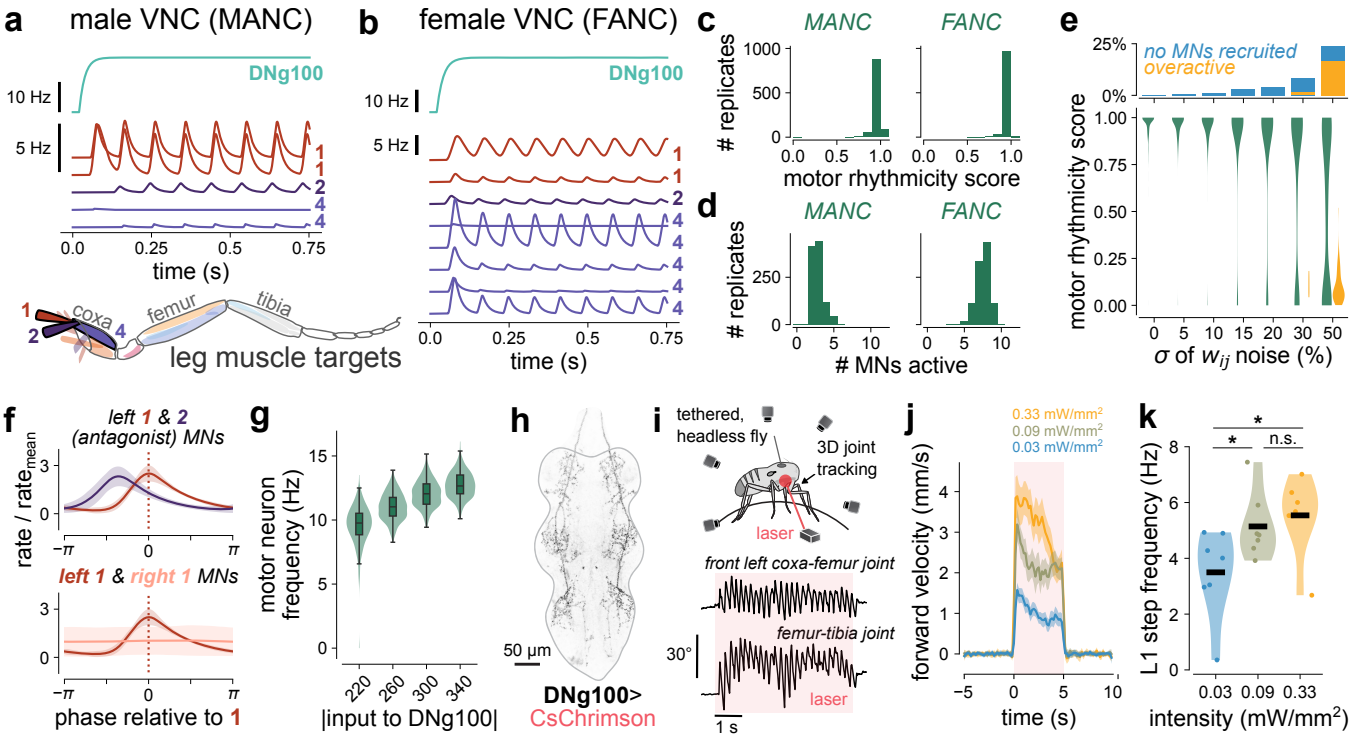

Figure 2: DNg100 produces rhythmic motor neuron activity in simulated connectome networks and headless flies. **a**, Example activity of MANC network with DNg100 activation. Selected motor neurons (MNs) are shown, with numbers corresponding to muscles they innervate in the anatomical diagram. **b**, Same as **a** for the FANC network. **c**, DNg100 activation consistently produced motor rhythms in MANC and FANC (n=1024 replicates). **d**, DNg100 typically recruited 2–5 motor neurons in MANC and 6–9 motor neurons in FANC (n=1024 replicates). **e**, Motor rhythms were robust to noise perturbations of weights of the connectivity matrix up to 10% (n=512 replicates per noise condition). Increasing noise also decreased MN recruitment and lead to unstable simulations (*top*). **f**, When DNg100s were activated bilaterally, left coxa promotor and remotor MNs were activate with a reliable phase offset (*top*), but left vs right coxa promotor neurons had no consistent phase relationship (*bottom*). Each subplot shows mean ± std of motor neuron activities (n=1024 replicates) after aligning to the peak of MN 1 (promotor). **g**, Increasing amplitude of activation to DNg100 increased motor neuron oscillation frequency in MANC network (n=512 replicates per condition). Simulations with no active motor neurons were omitted. Green shaded regions are distributions of frequencies, and black bars indicate medians and quartiles. **h**, VNC expression of Split-Gal4 line labeling DNg100 neurons (DNg100>CsChrimson, [47]). **i**, Example coxa-femur and femur-tibia joint kinematics of front left leg during optogenetic activation of DNg100 neurons in a headless fly on a spherical treadmill. **j**, At higher optogenetic stimulus intensities, flies walked with higher forward velocity (mean ± 95% c.i., shown for three intensities, n=7 flies, 8 trials per fly). **k**, Stepping frequency of the left front leg increased with laser intensity (p = 0.032, 0.352, and 0.042 for paired t-tests comparing low-medium, medium-high, and low-high laser intensities, respectively).

that optogenetically activating DNg100 neurons is sufficient to drive walking in headless flies ([47], see also **Supplementary Video 1**), but different stimulus intensities were not explored. To test this prediction experimentally, we expressed CsChrimson in DNg100 neurons and then optogenetically activated them in decapitated flies on a spherical treadmill (**Fig. 2h–i**, **Supplementary Fig. 2**). We found that increasing the laser intensity led to an increase in forward velocity and stepping frequency (**Fig. 2j–k**). This experiment confirmed predictions from our connectome simulations and suggests that the oscillation frequency of the CPG for walking is controlled by the strength of descending input from DNg100.

A core CPG circuit of three interneurons

Our connectome simulations offered an opportunity to understand how sustained descending commands from DNg100 are transformed by the thousands of cells in the VNC network into rhythmic motor activity. The circuitry linking DNg100 to leg motor neurons is extensive and highly recurrent (**Fig. 3a**), so understanding this transformation would be challenging using conventional connectome analyses that trace feedforward pathways.

To identify a minimal circuit capable of rhythm generation, we started from VNC network simulations with DNg100 activation, just as in **Fig. 2**, and designed a computational sufficiency screen. At each iteration of this screen, we stochastically silenced one interneuron, selected with a probability inversely proportional to its activity. If leg motor oscillations persisted (rhythmicity score >0.5), that cell was pruned from the network (**Fig. 3b**, see Methods for additional details). However, if the oscillations ceased (rhythmicity <0.5), the cell remained in the network. Each replicate of the screen terminated when none of the remaining cells could be silenced without disrupting leg motor neuron rhythms. The goal of the screen was to prune the network to a minimal, core subcircuit sufficient to generate leg motor rhythms in response to sustained DNg100 activity.

Independent computational sufficiency screens repeatedly converged to a minimal circuit of just three neurons, two excitatory and one inhibitory (**Fig. 3c**, in MANC, 636/1024 (62.1%) pruning screens converged to this same circuit). These three cells, which we refer to as "E1" (IN17A001), "E2" (INXXX466), and "I1" (IN16B036) for clarity, are interneurons local to the front left leg neuropil. The same approach applied to the FANC network converged to a circuit of four interneurons (70.4% of 1024 pruning screens), which also included E1 and E2, but identified a different inhibitory neuron "I2" (IN19A007) and one additional excitatory interneuron "E3" (IN19B012). Although several other solutions were found by the pruning screens, the minimal circuits nearly always included both E1 and E2 (**Fig. 3c–d**). A detailed list of the circuits and cells identified by the pruning screens are found in **Supplementary Tables 2 and 3**.

In the minimal three-neuron circuit, E1, E2, and I1 are connected all-to-all, but with particularly strong connections E1→E2, E2→I1, I1→E1, and I1→E2 (**Fig. 3f**). Only E1 receives direct synaptic input from DNg100. Thus, the predominant mechanism for rhythm generation is that DNg100 drives E1 to excite E2, amplifying the excitation, and E2 then recruits I1 to inhibit both excitatory neurons after some delay (corresponding to the time-constant parameter τ in our model). Since I1 does not receive any direct input from DNg100, E1 is disinhibited after the drive to I1 is released. This pattern of activity repeats cyclically as long as DNg100 provides excitation. A model of this three-neuron circuit that retains only the E1→E2, E2→I1, and I1→E1 connections still produced oscillatory activity (**Supplementary Fig. 3b**). All of the excitatory cells in the circuit connect to multiple motor neurons that innervate muscles throughout the leg (**Fig. 3f**). Thus, the differential patterns of excitation produced by E1 and E2 activate motor neurons at consistent phase offsets relative to each other (**Fig. 3g**).

In further support of our numerical simulation results, an eigendecomposition of the linearized dynamical system corresponding to the three-neuron model has one complex-conjugate pair of eigenvalues with an oscillation frequency of ∼14 cycles per second (**Supplementary Fig. 4a**). To confirm that our results do not rely on the specifics of a firing-rate model, we simulated the same circuit with leaky integrate-and-fire neurons and found similar patterns of rhythmic spiking activity (**Supplementary Fig. 5**).

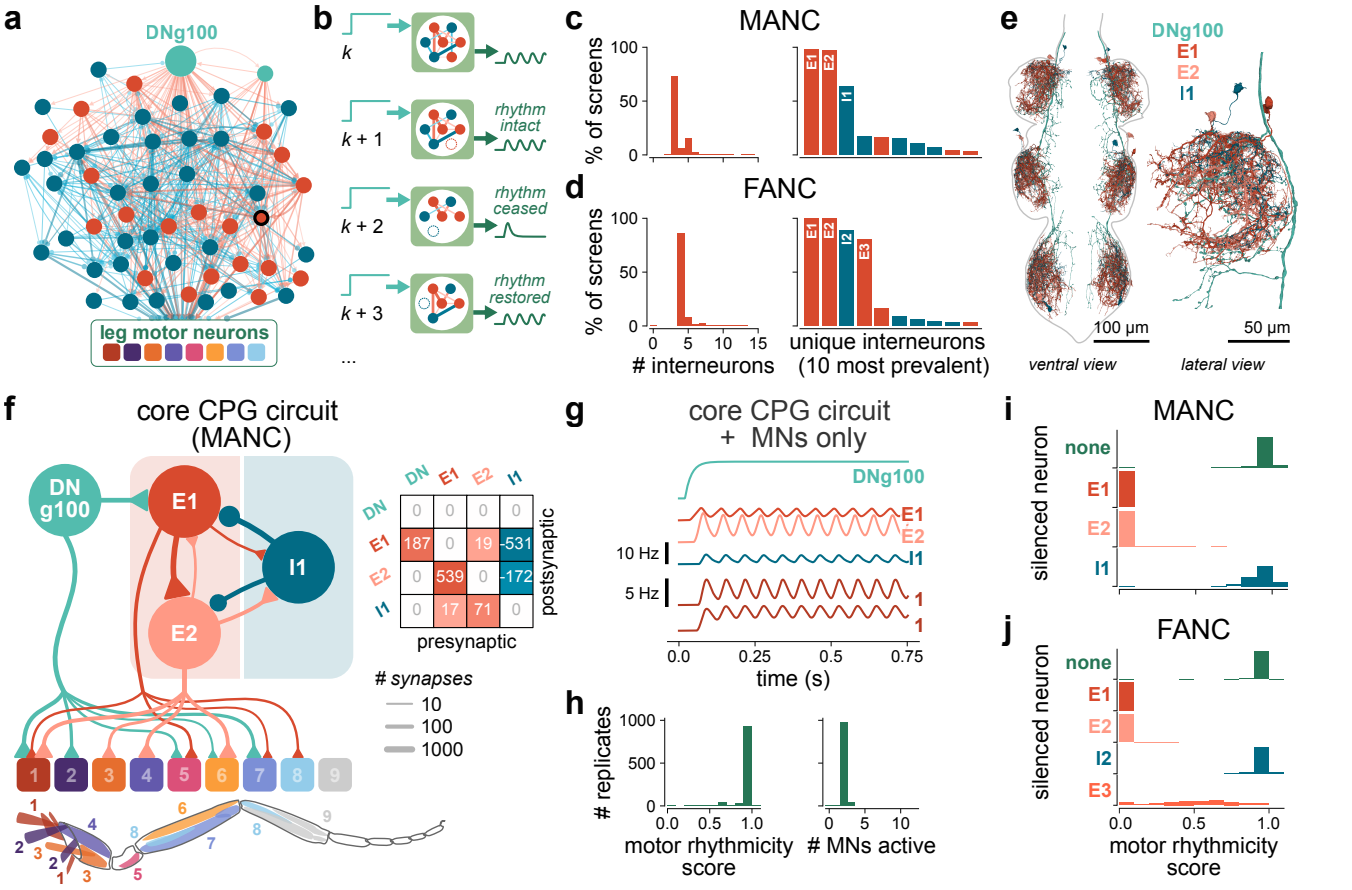

Figure 3: A computational sufficiency screen isolates a core CPG circuit downstream of DNg100 of three neurons per leg. **a**, Premotor network downstream of DNg100 in MANC. Shown are all neurons that receive at least 10 synapses from left DNg100 and make at least 10 synapses onto any left front leg motor neuron. Red cells are putative excitatory (cholinergic), blue cells are inhibitory (GABAergic or glutamatergic). The E1 cell is outlined in black. **b**, Schematic of iterative pruning procedure under DN input (teal). At each iteration, we remove one cell (dashed outlines) stochastically and evaluate the motor rhythmicity. This procedure terminates at a minimal circuit when no further neurons can be pruned without the rhythmicity score dropping below 0.5 (evaluated on MN output, green traces). **c**, Minimal circuits identified by pruning screens (n=1024 replicates, left DNg100, MANC). *Left*: Number of interneurons that in minimal circuits (5 screens did not converge to 15 or fewer interneurons and are not shown). *Right*: Percentage of screens in which minimal circuits contained unique interneurons (see Supplementary Table 2 for full list of cell identities). **d**, Same as **c**, but for FANC (1 outlier of 18 interneurons not shown). See Supplementary Table 3 for full list of cell identities. **e**, Anatomy of the core CPG circuit neurons (MANC). **f**, The core CPG circuit in MANC and its connectivity to motor neurons (shown are connections of at least 10 synapses). Triangles and circles are excitatory and inhibitory connections, respectively. Rounded boxes depict modules of motor neurons grouped by leg muscle innervation [30], illustrated on the leg schematic below. Synapse counts are summed across MNs within each module. Inset shows core CPG weight matrix. **g**, DNg100 activation of the core CPG circuit produced rhythmic activity in interneurons *Top* and leg motor neurons *Bottom*. **h**, DNg100 activation consistently produced motor rhythms (n = 1024 replicates). **i–j**, In the full network simulations, individually silencing E1 and E2 abolished leg motor rhythms, but silencing I1 (MANC), or I2 and E3 (FANC) did not.

The E1-E2-I1 circuit is sufficient, and both E1 and E2 are necessary, to produce leg motor rhythms in response to DNg100 activation. Motor rhythmicity scores of the three-neuron circuit were comparable to the full VNC network across independent simulation replicates (**Fig. 3h**). Unlike in the full network, increasing input magnitude to DNg100 in the three-neuron circuit does not change the frequency of motor neuron oscillations (**Supplementary Fig. 3a**). Silencing either E1 or E2 in the full VNC network models abolished all rhythmic activity (**Fig. 3i**). This necessity is consistent with the fact that E1 and E2 were present in nearly all circuits from the pruning screen, across multiple legs and both connectome datasets (**Fig. 3c–d, Supplementary Figs. 6 and 7**). The circuit requires strong inhibition, but the identity of the inhibitory cell is not unique across replicates of the pruning screen. I1 and I2 were not necessary in the full MANC and FANC network models respectively (**Fig. 3i**), where inhibition from either neuron was compensated for by other redundant inhibitory neurons.

The minimal three-neuron CPG circuit is repeated in the neuropils of all six legs of both connectomes (**Fig. 3e, Supplementary Fig. 8**), suggesting the presence of a conserved circuit motif for rhythm generation across leg segments. Because neurons in our model lack intrinsic bursting properties, we propose that the walking rhythm can be generated by a network oscillator mechanism. Taken together, our modeling results support the hypothesis that E1-E2-I1 form the core of a CPG circuit for forward walking in each leg neuropil.

A separate class of descending neurons recruits an overlapping rhythm-generating circuit

Having isolated a CPG circuit downstream of DNg100, we returned to examine the other DNs that generated leg motor rhythms from our initial computational screen. One cell type, DNb08, stood out because it consists of four neurons (two per side) that all produced high rhythmicity scores (**Fig. 1e**, **Supplemental Table 1**). Although a study had created genetic driver lines for DNb08 neurons [51], their function had not been previously investigated. Similar to DNg100, we found that activating one DNb08 neuron in the full network simulation consistently produced rhythmic activity in multiple leg motor neurons (**Fig. 4a–b**). In an experiment that tested these model predictions, we found that optogenetically activating DNb08 cells in decapitated flies produced rhythmic leg movements (**Fig. 4c–e**, **Supplementary Video 2**). These movements were different from the coordinated walking pattern of DNg100 stimulation—they resembled the searching or flailing movements that insects exhibit when their legs are not in contact with the ground [52]. Indeed, DNb08 evoked leg movements more reliably when the spherical treadmill was removed and the legs were not in contact with the substrate. Overall, these results illustrate how network simulations can predict the motor function of previously unstudied cell types from the connectome.

To isolate the core circuit that generates rhythmic activity downstream of DNb08, we repeated our computational sufficiency screen. In nearly half (45.4%) of the 1024 replicates, the screen converged to a circuit of five interneurons (**Fig. 4f**). This most common minimal circuit included the same E1 and E2 neurons from the core walking CPG, in addition to two other excitatory neurons "E4" (IN03A006) and "E5" (INXXX466) and an inhibitory neuron I2 (IN19A007); see **Fig. 4g–h** and **Supplementary Table 4**. Unlike DNg100, DNb08 is only weakly presynaptic to E1, but E4 and E5 are both postsynaptic to DNb08 and provide strong input to E1. I2 provides strong feedback inhibition onto all four excitatory interneurons. Thus, the primary mechanism for rhythm generation is the same as in the core walking CPG circuit, where several mutually excitatory neurons activate an inhibitory neuron after some delay, which then strongly inhibits all of the excitatory neurons. Silencing each of the excitatory neurons (E1, E2, E4, E5) in the full network severely degraded rhythmic motor patterns, but silencing I2 did not (**Fig. 4i**). The overlap between the DNg100 and DNb08 minimal CPG circuits suggests that DNs supporting different behaviors recruit overlapping subnetworks that share a core rhythm-generating mechanism.

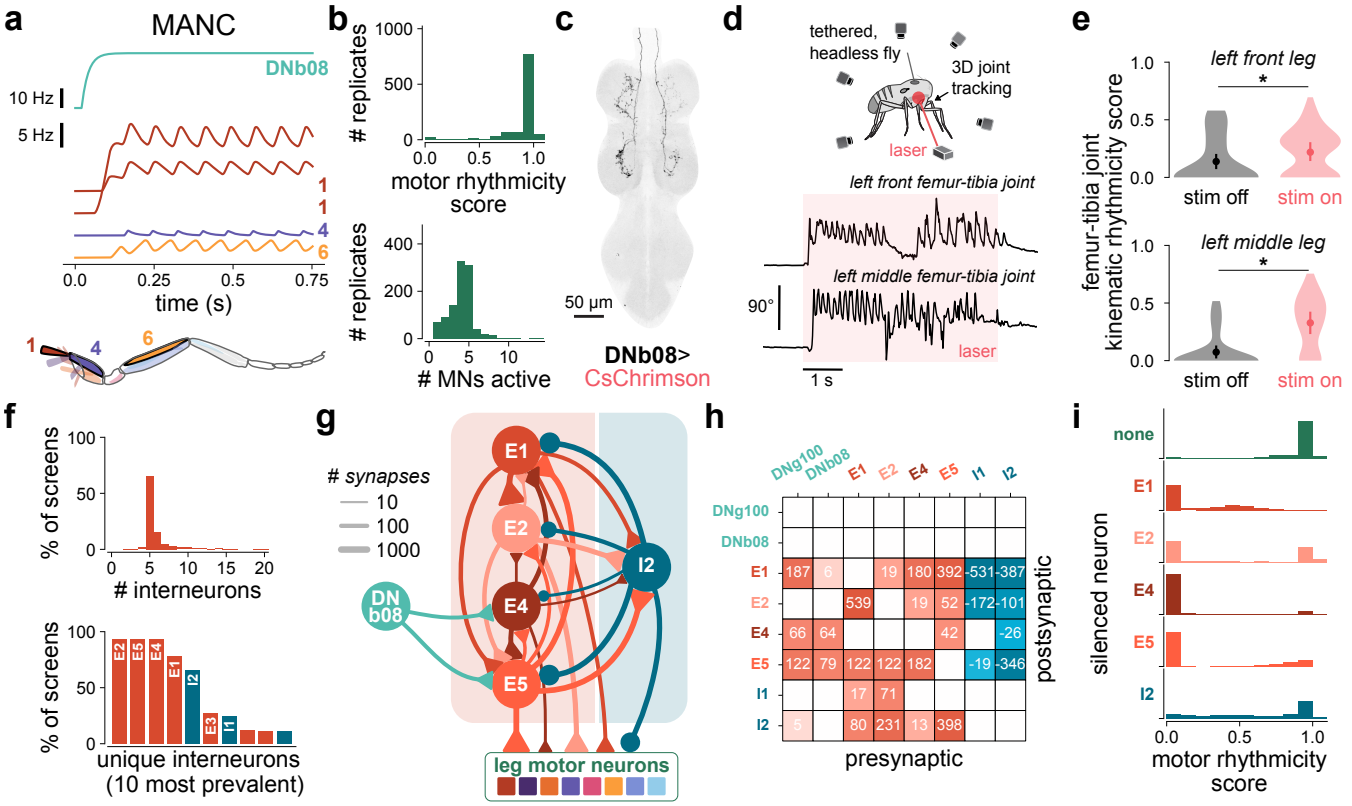

Figure 4: DNb08 produces rhythmic leg movements in simulations and headless flies, and its downstream network converges to an overlapping minimal circuit. **a**, Activation of DNb08 in the full MANC network produced rhythm leg motor activity. All active motor neurons are shown. Muscle innervation of MNs are indicated below. **b**, DNb08 activation consistently produced leg motor rhythms (n=1024 replicates). **c**, VNC expression of Split-gal4 line labeling DNb08 neurons (SS70620>CsChrimson). **d**, Femur-tibia joint kinematics in front and middle legs during optogenetic activation of DNb08 neurons in headless flies (see **Supplementary Video 2**). **e**, Activating DNb08 produced oscillatory movement of the front and middle legs (n=10 flies, 8 stim-on and 4 stim-off trials per fly). Mean and error bars (95% c.i.) computed across means of individual flies (p = 0.036, 0.004 for paired t-tests comparing stimulus on vs. off trials for front and middle leg, respectively). Violin plots show overall distributions over all trials. **f**, Minimal circuits identified by pruning. *Top*: Number of interneurons within minimal circuits across 1024 independent simulations (32 screens did not converge to 20 or fewer interneurons and are not shown). Bottom: Percentage of screens in which minimal circuits contained specified interneurons (see **Supplementary Table 4** for full list of cell identities). **g**, Connectivity of the minimal rhythm-generating circuit downstream of DNb08 (MANC). Triangles and circles indicate excitatory and inhibitory connections, respectively. Synapse counts are summed across all left leg motor neurons. **h**, Synaptic weight matrix for all cells identified in either DNg100 and DNb08 minimal circuits (MANC) reveals strong shared circuitry (E1 and E2) and a common motif of excitatory-inhibitory connections. **i**, In full MANC network simulations, individually silencing E1, E2, E4, and E5 abolished leg motor rhythms, but silencing I2 did not.

Discussion

A putative CPG circuit for fly walking

By simulating the dynamics of *Drosophila* VNC connectomes, we identified a putative central pattern generator (CPG) circuit for walking that consists of three neurons (**Fig. 3f**). Each DNg100 neuron synapses onto more than 1400 cells in the VNC, which would have made it prohibitively difficult to pinpoint a CPG circuit using traditional connectivity analyses. We isolated the core CPG circuit with a computational sufficiency screen that iteratively pruned the VNC network downstream of DNg100 while preserving leg motor neuron rhythms. The three core CPG neurons and their synaptic connectivity patterns are repeated in each of the six leg neuropils and across multiple connectomes of the fly VNC. Computational pruning of the network downstream of DNb08, a separate pathway that we found also drives rhythmic leg movements, converged on a five-neuron circuit that included the same two excitatory neurons present in the core CPG. From the connectome, we see that the interneurons identified by our computational pruning screens receive input from other walking-related descending neurons, including DNg97 (oDN1, [47]) and DNg74 (web, [53]), as well as grooming-related neurons DNg12 [54] and DNg62 (aDN1, [55]) (see **Supplementary Table 5**). Based on this convergence, we hypothesize that many rhythmic limbed behaviors rely on the same core CPG in each leg. In other words, we suggest that multiple motor patterns are generated in the fly VNC by modulating the frequency and phase of the core CPG circuit, sometimes by recruiting additional cells, rather than switching among multiple, non-overlapping CPGs. This idea is consistent with past work showing that pattern-generating circuits are multifunctional [56, 57], in that the same neurons can participate in the generation of different behaviors.

Our simulation results make a suite of predictions that motivate future experiments. Here, we carried out feasible experiments using existing genetic reagents, which confirmed that DNg100 activity controls walking speed (**Fig. 2i–k**) and that activation of DNb08 drives rhythmic leg movements (**Fig. 4d–e**). Further experiments will require the creation of new genetic driver lines that specifically label the interneurons in the core CPG circuit. Our simulations predict that optogenetically silencing E1 and/or E2 neurons will abolish rhythmic leg movements driven by DNg100. In contrast, in addition to I1, there exist multiple inhibitory cells, with similar connectivity onto E1 and E2, that are likely sufficient to produce rhythmic inhibitory feedback in the CPG network. Electrophysiological recordings will be required to test whether these cells exhibit nonlinear membrane properties (e.g., intrinsic bursting, plateau potentials, post-inhibitory rebound) that have been found in other CPG circuits. The cells in our model did not possess any of these properties, suggesting that the core CPG can operate as a network oscillator. However, it is also possible that cells in the circuit are intrinsically bursting or possess other membrane properties that contribute to rhythm generation.

Limitations and future extensions of the model

Activating DNg100 neurons in our connectome simulations recruited motor neurons that innervate muscles throughout the fly leg. Some muscle pairs were activated with naturalistic phase relationships. For example, during forward walking, the coxa promotor muscle swings the leg anteriorly during the swing phase, while the coxa remotor moves the leg posteriorly during stance. In our simulations, these antagonistic muscles displayed a phase offset that resembles that recorded in other walking insects [5]. However, other key muscles likely active during walking were either silent or non-rhythmic (e.g., the main tibia flexors [46]). This suggests that although the feedforward signals from the CPG circuit may be sufficient to initiate cyclic stepping movements, the naturalistic pattern of muscle activation likely relies on additional factors, including proprioceptive feedback, mechanical coupling, activity of other DNs, or neuromodulation. This idea is consistent with extensive evidence that feedforward CPG rhythms and sensory feedback act cooperatively during locomotion [6, 58].

In the full DNg100 network model, the frequency of the motor rhythms of the legs increased with

higher magnitudes of DNg100 activation, a prediction that we confirmed experimentally using optogenetic manipulations in behaving flies. However, the minimal three-neuron CPG model did not exhibit frequency modulation. In the future, it may be possible to use extensions of computational sufficiency screens to identify larger circuits that support frequency modulation and other higher-order network properties.

Our DNg100 simulations did not produce the tripod inter-leg coordination pattern characteristic of hexapod walking. Several VNC neurons connect the left and right CPG circuits, but their inclusion in our simulations was insufficient to couple the phase of the left and right legs. Additional proprioceptive feedback, biomechanical coupling, or other neural pathways may be necessary to organize stepping phase and produce tripod-like interleg coordination. In the future, it may be possible to test these hypotheses by coupling VNC connectome simulations to control and receive feedback from biomechanical models of the fly body interacting with a simulated physical environment [59, 60]. Such an extension would require adding biologically realistic interfaces of proprioceptive sensors and muscle actuators. DNs are also recruited as populations, due to high levels of interconnectivity in the brain [61], so future models could incorporate connectivity between DNs within the brain using the recent *Drosophila* brain and nerve cord (BANC) connectome dataset [62].

Theory of minimal rhythm-generating networks

In a neural network constructed with basic threshold-linear units, a three-neuron circuit consisting of two excitatory cells and one inhibitory cell is a mathematically minimal model for rhythm generation. Similar minimal networks were studied in early neural network theory by Amari [63], who showed that a limit cycle solution emerges within a specific regime of synaptic weights between a pair of cells, one excitatory and one inhibitory. In this minimal two-neuron circuit, the excitatory cell must excite itself (i.e., via autapses). Because neurons in the fly CNS rarely form autapses [28, 27], a minimum of two excitatory cells that excite each other are necessary [64], as we found in our three-neuron CPG circuit. Further, for oscillations to emerge, the circuit must provide inhibition onto excitatory units; all minimal circuits our pruning screen identified followed this same architecture, including the five-neuron circuit downstream of DNb08. Beyond minimal rhythm-generating networks, larger inhibition-dominated circuits may be designed to support flexible motor patterns, such as distinct gaits [65] and variable oscillatory network dynamics [66].

The mathematical mechanism by which the three-neuron CPG circuit generates rhythms is closely related to oscillatory networks of coupled non-neural biological components, including evolved and synthetic gene circuits. For example, circadian rhythms in cyanobacteria are maintained by three genes, the *kaiABC* cluster, which form a pacemaker through positive and negative feedback interactions [67]. In synthetic biology, the oscillator circuit known as the *repressilator* combines three transcriptional regulators, in this case arranged to cyclically inhibit each other [68]. Another oscillatory circuit with tunable periodicity was designed with two transcriptional regulators, one self-activating unit that also activates an inhibitory unit, which in turn inhibits the first [69]. Similar to our three-neuron circuit, where the E1-E2 connection may be crucial in amplifying DNg100 excitation and introducing a time delay in activation, these genetic circuits require time-delayed feedback to produce oscillations.

Connectome simulations as a discovery tool

Beyond walking, our simulation approach may be used to discover functional microcircuits in other connectomes that produce specific patterns of neural dynamics. A key consideration in designing such computational simulations is the interpretability of the model's inputs and outputs. The outputs of our simulations were leg motor neuron firing rates, which are closely related to motor behavior, thus allowing us to test predictions from our simulations with optogenetic experiments in behaving flies. We were surprised that our modeling results were generally robust across a range of biophysical parameters and variation in synaptic connectivity. One reason may be that our criteria for success, rhythmic activity of leg motor neurons, was quite permissive. Another reason may be that the core CPG circuit is hardwired to operate robustly across a wide range of environmental conditions and behavioral contexts [70].

To investigate ethological behaviors where movements are coordinated over longer timescales than a single walking bout, connectome simulations may need to incorporate other circuit and cellular parameters such as receptor and ion channel expression, neuronal morphology, neuromodulation, and plasticity. Machine-learning approaches, such as reinforcement learning, may also help fine-tune connectome simulations to achieve more complex motor patterns and behavioral sequences embodied in a biomechanical fly body model (as was done with artificial neural networks in [71] and [60]). Overall, our work shows that network simulations, when pursued in close collaboration with biological experiments, can predict circuit dynamics from static connectomics and are a compelling approach to study the neuronal control of animal behavior.

Acknowledgements

We thank Eiman Azim, Steve Brunton, Michael Dickinson, Michael Elowitz, David Perkel, Adriane Otopalik, Simon Sponberg, and members of the Tuthill and Brunton Labs for comments on the manuscript. We thank Anne Sustar for the VNC images in Fig. 4 and Tony Azevedo for advice on motor neuron modeling, David Samy for help with coding, Salil Bidaye for sharing fly stocks and confocal images, Kenji Doya for pointing us to Amari's 1978 textbook in Japanese and Tomo Ouchi for assistance with translating it. This work was funded through a Swartz Foundation Fellowship in Theoretical Neuroscience to E.T.T.A.; a Shanahan Family Foundation Fellowship at the Interface of Data and Neuroscience to D.T.; National Institutes of Health grants R01NS102333, R01NS128785, the New York Stem Cell Foundation, and a Pew Biomedical Scholar Award to J.C.T.; Air Force Office of Scientific Research award FA9550-19-1-0386, NIH grants U01NS136507, R01NS136988, and the Richard & Joan Komen University Chair to B.W.B. J.C.T is a New York Stem Cell Foundation – Robertson Investigator.

Author Contributions

S.M.P., J.C.T., and B.W.B. conceived the study, designed the analyses, and wrote the manuscript. S.M.P. designed and developed models for connectome simulation, with assistance from J.K.L., and E.T.T.A. implemented software simulations in JAX. G.M.C. collected and analyzed behavioral data. D.T. derived the dynamical systems analysis and developed the leaky integrate-and-fire neural model.

Data and Code Availability

All code to run the connectome simulations, results from computational experiments, and scripts to reproduce the analyses are available on GitHub (`https://github.com/smpuglie/Pugliese_cpg_2025`).

References

[1] C. S. Sherrington, *The integrative action of the nervous system.* New Haven Yale University Press, 1920.

[2] T. G. Brown, "On the nature of the fundamental activity of the nervous centres; together with an analysis of the conditioning of rhythmic activity in progression, and a theory of the evolution of function in the nervous system," *The Journal of Physiology*, vol. 48, pp. 18–46, Mar. 1914.

[3] G. M. Hughes and C. A. G. Wiersma, "The Co-ordination of Swimmeret Movements in the Crayfish, Procambarus Clarkii (Girard)," *Journal of Experimental Biology*, vol. 37, pp. 657–670, Dec. 1960.

[4] D. M. Wilson, "The central nervous control of flight in a locust," *Journal of Experimental Biology*, vol. 38, pp. 471–490, June 1961.

[5] A. Büschges and J. M. Ache, "Motor control on the move: from insights in insects to general mechanisms," *Physiological Reviews*, vol. 105, no. 3, pp. 975–1031, 2025.

[6] M. Goulding, T. Bollu, and A. Büschges, "Sensory feedback and the dynamic control of movement," *Annual Review of Neuroscience*, 2025.

[7] S. Gosgnach, "The mammalian locomotor CPG: revealing the contents of the black box," *Journal of Neurophysiology*, vol. 133, no. 2, pp. 472–478, 2025.

[8] N. Daur, F. Nadim, and D. Bucher, "The complexity of small circuits: the stomatogastric nervous system," *Current Opinion in Neurobiology*, vol. 41, pp. 1–7, 2016.

[9] W. O. Friesen and W. B. Kristan, "Leech locomotion: swimming, crawling, and decisions," *Current Opinion in Neurobiology*, vol. 17, no. 6, pp. 704–711, 2007.

[10] R. L. Calabrese, B. J. Norris, and A. Wenning, "The neural control of heartbeat in invertebrates," *Current Opinion in Neurobiology*, vol. 41, pp. 68–77, 2016.

[11] C. A. Del Negro, G. D. Funk, and J. L. Feldman, "Breathing matters," *Nature Reviews Neuroscience*, vol. 19, no. 6, pp. 351–367, 2018.

[12] S. Grillner, "Biological Pattern Generation: The Cellular and Computational Logic of Networks in Motion," *Neuron*, vol. 52, pp. 751–766, Dec. 2006.

[13] G. M. Shepherd, S. Grillner, and P. S. Katz, "The Tritonia swim central pattern generator," in *Handbook of Brain Microcircuits*, Oxford University Press, 12 2017.

[14] E. Marder and R. L. Calabrese, "Principles of rhythmic motor pattern generation," *Physiological Reviews*, vol. 76, no. 3, pp. 687–717, 1996.

[15] R. L. Calabrese and E. Marder, "Degenerate Neuronal and Circuit Mechanisms Important for Generating Rhythmic Motor Patterns," *Physiological Reviews*, June 2024.

[16] H. Lindén, P. C. Petersen, M. Vestergaard, and R. W. Berg, "Movement is governed by rotational neural dynamics in spinal motor networks," *Nature*, vol. 610, pp. 526–531, Oct. 2022.

[17] B. Strohmer, E. Najarro, J. Ausborn, R. W. Berg, and S. Tolu, "Sparse Firing in a Hybrid Central Pattern Generator for Spinal Motor Circuits," *Neural Computation*, vol. 36, pp. 759–780, Apr. 2024.

[18] S. H. Strogatz, "From Kuramoto to Crawford: exploring the onset of synchronization in populations of coupled oscillators," *Physica D: Nonlinear Phenomena*, vol. 143, pp. 1–20, Sept. 2000.

[19] M. Golubitsky, I. Stewart, P.-L. Buono, and J. J. Collins, "Symmetry in locomotor central pattern generators and animal gaits," *Nature*, vol. 401, pp. 693–695, Oct. 1999.

[20] J. Proctor and P. Holmes, "Reflexes and preflexes: on the role of sensory feedback on rhythmic patterns in insect locomotion," *Biological Cybernetics*, vol. 102, pp. 513–531, June 2010.

[21] L. Karashchuk, J. S. L. Li, G. M. Chou, S. Walling-Bell, S. L. Brunton, J. C. Tuthill, and B. W. Brunton, "Sensorimotor delays constrain robust locomotion in a 3D kinematic model of fly walking," *eLife*, vol. 13, Aug. 2024.

[22] M. Yao, A. Nagamori, S. C. Maçãs, E. Azim, T. Sharpee, M. Goulding, D. Golomb, and G. Gatto, "The spinal premotor network driving scratching flexor and extensor alternation," *Cell Reports*, vol. 44, no. 6, 2025.

[23] N. G. Hatsopoulos, "Coupling the Neural and Physical Dynamics in Rhythmic Movements," *Neural Computation*, vol. 8, pp. 567–581, Apr. 1996.

[24] A. J. Ijspeert, "Central pattern generators for locomotion control in animals and robots: A review," *Neural Networks*, vol. 21, pp. 642–653, May 2008.

[25] M. Shafiee, G. Bellegarda, and A. Ijspeert, "ManyQuadrupeds: Learning a Single Locomotion Policy for Diverse Quadruped Robots," in *2024 IEEE International Conference on Robotics and Automation (ICRA)*, pp. 3471–3477, May 2024.

[26] L. K. Scheffer, C. S. Xu, M. Januszewski, Z. Lu, S.-y. Takemura, K. J. Hayworth, G. B. Huang, K. Shinomiya, J. Maitlin-Shepard, S. Berg, J. Clements, P. M. Hubbard, W. T. Katz, L. Umayam, T. Zhao, D. Ackerman, T. Blakely, J. Bogovic, T. Dolafi, D. Kainmueller, T. Kawase, K. A. Khairy, L. Leavitt, P. H. Li, L. Lindsey, N. Neubarth, D. J. Olbris, H. Otsuna, E. T. Trautman, M. Ito, A. S. Bates, J. Goldammer, T. Wolff, R. Svirskas, P. Schlegel, E. Neace, C. J. Knecht, C. X. Alvarado, D. A. Bailey, S. Ballinger, J. A. Borycz, B. S. Canino, N. Cheatham, M. Cook, M. Dreher, O. Duclos, B. Eubanks, K. Fairbanks, S. Finley, N. Forknall, A. Francis, G. P. Hopkins, E. M. Joyce, S. Kim, N. A. Kirk, J. Kovalyak, S. A. Lauchie, A. Lohff, C. Maldonado, E. A. Manley, S. McLin, C. Mooney, M. Ndama, O. Ogundeyi, N. Okeoma, C. Ordish, N. Padilla, C. M. Patrick, T. Paterson, E. E. Phillips, E. M. Phillips, N. Rampally, C. Ribeiro, M. K. Robertson, J. T. Rymer, S. M. Ryan, M. Sammons, A. K. Scott, A. L. Scott, A. Shinomiya, C. Smith, K. Smith, N. L. Smith, M. A. Sobeski, A. Suleiman, J. Swift, S. Takemura, I. Talebi, D. Tarnogorska, E. Tenshaw, T. Tokhi, J. J. Walsh, T. Yang, J. A. Horne, F. Li, R. Parekh, P. K. Rivlin, V. Jayaraman, M. Costa, G. S. Jefferis, K. Ito, S. Saalfeld, R. George, I. A. Meinertzhagen, G. M. Rubin, H. F. Hess, V. Jain, and S. M. Plaza, "A connectome and analysis of the adult Drosophila central brain," *eLife*, vol. 9, p. e57443, Sept. 2020.

[27] S.-y. Takemura, K. J. Hayworth, G. B. Huang, M. Januszewski, Z. Lu, E. C. Marin, S. Preibisch, C. S. Xu, J. Bogovic, A. S. Champion, H. S. Cheong, M. Costa, K. Eichler, W. Katz, C. Knecht, F. Li, B. J. Morris, C. Ordish, P. K. Rivlin, P. Schlegel, K. Shinomiya, T. Stürner, T. Zhao, G. Badalamente, D. Bailey, P. Brooks, B. S. Canino, J. Clements, M. Cook, O. Duclos, C. R. Dunne, K. Fairbanks, S. Fang, S. Finley-May, A. Francis, R. George, M. Gkantia, K. Harrington, G. P. Hopkins, J. Hsu, P. M. Hubbard, A. Javier, D. Kainmueller, W. Korff, J. Kovalyak, D. Krzemiński, S. A. Lauchie, A. Lohff, C. Maldonado, E. A. Manley, C. Mooney, E. Neace, M. Nichols, O. Ogundeyi, N. Okeoma, T. Paterson, E. Phillips, E. M. Phillips, C. Ribeiro, S. M. Ryan, J. T. Rymer, A. K. Scott, A. L. Scott, D. Shepherd, A. Shinomiya, C. Smith, N. Smith, A. Suleiman, S. Takemura, I. Talebi, I. F. Tamimi, E. T. Trautman, L. Umayam, J. J. Walsh, T. Yang, G. M. Rubin, L. K. Scheffer, J. Funke, S. Saalfeld, H. F. Hess, S. M. Plaza, G. M. Card, G. S. Jefferis, and S. Berg, "A connectome of the male Drosophila ventral nerve cord," *eLife*, May 2024.

[28] A. Azevedo, E. Lesser, J. S. Phelps, B. Mark, L. Elabbady, S. Kuroda, A. Sustar, A. Moussa, A. Khandelwal, C. J. Dallmann, S. Agrawal, S.-Y. J. Lee, B. Pratt, A. Cook, K. Skutt-Kakaria, S. Gerhard, R. Lu, N. Kemnitz, K. Lee, A. Halageri, M. Castro, D. Ih, J. Gager, M. Tammam, S. Dorkenwald, F. Collman, C. Schneider-Mizell, D. Brittain, C. S. Jordan, M. Dickinson, A. Pacureanu, H. S. Seung, T. Macrina, W.-C. A. Lee, and J. C. Tuthill, "Connectomic reconstruction of a female Drosophila ventral nerve cord," *Nature*, vol. 631, pp. 360–368, July 2024.

[29] S. Dorkenwald, A. Matsliah, A. R. Sterling, P. Schlegel, S.-c. Yu, C. E. McKellar, A. Lin, M. Costa, K. Eichler, Y. Yin, W. Silversmith, C. Schneider-Mizell, C. S. Jordan, D. Brittain, A. Halageri, K. Kuehner, O. Ogedengbe, R. Morey, J. Gager, K. Kruk, E. Perlman, R. Yang, D. Deutsch, D. Bland, M. Sorek, R. Lu, T. Macrina, K. Lee, J. A. Bae, S. Mu, B. Nehoran, E. Mitchell, S. Popovych, J. Wu, Z. Jia, M. A. Castro, N. Kemnitz, D. Ih, A. S. Bates, N. Eckstein, J. Funke, F. Collman, D. D. Bock, G. S. X. E. Jefferis, H. S. Seung, and M. Murthy, "Neuronal wiring diagram of an adult brain," *Nature*, vol. 634, pp. 124–138, Oct. 2024.

[30] E. Lesser, A. W. Azevedo, J. S. Phelps, L. Elabbady, A. Cook, D. Sakeena Syed, B. Mark, S. Kuroda, A. Sustar, A. Moussa, C. J. Dallmann, S. Agrawal, S.-Y. J. Lee, B. Pratt, K. Skutt-Kakaria, S. Gerhard, R. Lu, N. Kemnitz, K. Lee, A. Halageri, M. Castro, D. Ih, J. Gager, M. Tammam, S. Dorkenwald, F. Collman, C. Schneider-Mizell, D. Brittain, C. S. Jordan, T. Macrina, M. Dickinson, W.-C. A. Lee, and J. C. Tuthill, "Synaptic architecture of leg and wing premotor control networks in Drosophila," *bioRxiv*, p. 2023.05.30.542725, Apr. 2024.

[31] T. Stürner, P. Brooks, L. Serratosa Capdevila, B. J. Morris, A. Javier, S. Fang, M. Gkantia, S. Cachero, I. R. Beckett, E. C. Marin, *et al.*, "Comparative connectomics of Drosophila descending and ascending neurons," *Nature*, pp. 1–15, 2025.

[32] E. C. Marin, B. J. Morris, T. Stürner, A. S. Champion, D. Krzeminski, G. Badalamente, M. Gkantia, C. R. Dunne, K. Eichler, S.-y. Takemura, I. F. Tamimi, S. Fang, S. S. Moon, H. S. Cheong, F. Li, P. Schlegel, S. E. Ahnert, S. Berg, G. M. Card, M. Costa, D. Shepherd, and G. S. Jefferis, "Systematic annotation of a complete adult male Drosophila nerve cord connectome reveals principles of functional organisation," *eLife*, July 2024.

[33] C. I. Bargmann and E. Marder, "From the connectome to brain function," *Nature Methods*, vol. 10, pp. 483–490, June 2013.

[34] L. K. Scheffer and I. A. Meinertzhagen, "A connectome is not enough – what is still needed to understand the brain of Drosophila?," *Journal of Experimental Biology*, vol. 224, p. jeb242740, Oct. 2021.

[35] P. K. Shiu, G. R. Sterne, N. Spiller, R. Franconville, A. Sandoval, J. Zhou, N. Simha, C. H. Kang, S. Yu, and J. S. Kim, "A Drosophila computational brain model reveals sensorimotor processing," *Nature*, vol. 634, no. 8032, pp. 210–219, 2024.

[36] J. K. Lappalainen, F. D. Tschopp, S. Prakhya, M. McGill, A. Nern, K. Shinomiya, S.-y. Takemura, E. Gruntman, J. H. Macke, and S. C. Turaga, "Connectome-constrained networks predict neural activity across the fly visual system," *Nature*, vol. 634, pp. 1132–1140, Oct. 2024.

[37] B. R. Cowley, A. J. Calhoun, N. Rangarajan, E. Ireland, M. H. Turner, J. W. Pillow, and M. Murthy, "Mapping model units to visual neurons reveals population code for social behaviour," *Nature*, vol. 629, pp. 1100–1108, May 2024.

[38] S. Duan, L. L. Dong, and I. Fiete, "From synapses to dynamics: Obtaining function from structure in a connectome constrained model of the head direction circuit," *bioRxiv*, pp. 2025–05, 2025.

[39] K. G. Pearson and C. R. Fourtner, "Nonspiking interneurons in walking system of the cockroach," *Journal of Neurophysiology*, vol. 38, pp. 33–52, Jan. 1975.

[40] M. Burrows, "The control of sets of motoneurones by local interneurones in the locust.," *The Journal of Physiology*, vol. 298, no. 1, pp. 213–233, 1980.

[41] A. Büschges, "Role of local nonspiking interneurons in the generation of rhythmic motor activity in the stick insect," *Journal of Neurobiology*, vol. 27, no. 4, pp. 488–512, 1995.

[42] S. Agrawal, E. S. Dickinson, A. Sustar, P. Gurung, D. Shepherd, J. W. Truman, and J. C. Tuthill, "Central processing of leg proprioception in *Drosophila*," *eLife*, vol. 9, p. e60299, dec 2020.

[43] A. A. Prinz, C. P. Billimoria, and E. Marder, "Alternative to hand-tuning conductance-based models: construction and analysis of databases of model neurons," *Journal of Neurophysiology*, 2003.

[44] N. W. Gouwens and R. I. Wilson, "Signal Propagation in Drosophila Central Neurons," *Journal of Neuroscience*, vol. 29, pp. 6239–6249, May 2009.

[45] K. S. Kakaria and B. L. de Bivort, "Ring Attractor Dynamics Emerge from a Spiking Model of the Entire Protocerebral Bridge," *Frontiers in Behavioral Neuroscience*, vol. 11, Feb. 2017.

[46] A. W. Azevedo, E. S. Dickinson, P. Gurung, L. Venkatasubramanian, R. S. Mann, and J. C. Tuthill, "A size principle for recruitment of Drosophila leg motor neurons," *eLife*, vol. 9, p. e56754, 2020.

[47] N. Sapkal, N. Mancini, D. S. Kumar, N. Spiller, K. Murakami, G. Vitelli, B. Bargeron, K. Maier, K. Eichler, G. S. X. E. Jefferis, P. K. Shiu, G. R. Sterne, and S. S. Bidaye, "Neural circuit mechanisms underlying context-specific halting in Drosophila," *Nature*, vol. 634, pp. 191–200, Oct. 2024.

[48] J. Buhmann, A. Sheridan, C. Malin-Mayor, P. Schlegel, S. Gerhard, T. Kazimiers, R. Krause, T. M. Nguyen, L. Heinrich, W.-C. A. Lee, R. Wilson, S. Saalfeld, G. S. X. E. Jefferis, D. D. Bock, S. C. Turaga, M. Cook, and J. Funke, "Automatic detection of synaptic partners in a whole-brain Drosophila electron microscopy data set," *Nature Methods*, vol. 18, pp. 771–774, July 2021.

[49] B. D. DeAngelis, J. A. Zavatone-Veth, and D. A. Clark, "The manifold structure of limb coordination in walking Drosophila," *eLife*, vol. 8, p. e46409, June 2019.

[50] B. G. Pratt, S.-Y. J. Lee, G. M. Chou, and J. C. Tuthill, "Miniature linear and split-belt treadmills reveal mechanisms of adaptive motor control in walking Drosophila," *Current Biology*, vol. 34, pp. 4368–4381.e5, Oct. 2024.

[51] J. L. Zung, S. Namiki, G. W. Meissner, H. S. J. Cheong, M. Costa, K. Eichler, T. Stürner, G. S. X. E. Jefferis, C. Managan, F. P. Team, W. Korff, and G. M. Card, "An updated catalogue of split-GAL4 driver lines for descending neurons in Drosophila melanogaster," Apr. 2025.

[52] E. M. Berg, S. L. Hooper, J. Schmidt, and A. Büschges, "A leg-local neural mechanism mediates the decision to search in stick insects," *Current Biology*, vol. 25, no. 15, pp. 2012–2017, 2015.

[53] C. J. Dallmann, Y. Luo, S. Agrawal, G. M. Chou, A. Cook, B. W. Brunton, and J. C. Tuthill, "Presynaptic inhibition selectively suppresses leg proprioception in behaving Drosophila," *bioRxiv*, pp. 2023–10, 2023.

[54] L. Guo, N. Zhang, and J. H. Simpson, "Descending neurons coordinate anterior grooming behavior in Drosophila," *Current Biology*, vol. 32, pp. 823–833.e4, Feb. 2022.

[55] S. Hampel, R. Franconville, J. H. Simpson, and A. M. Seeds, "A neural command circuit for grooming movement control," *eLife*, vol. 4, p. e08758, Sept. 2015.

[56] K. L. Briggman and W. B. K. Jr, "Multifunctional Pattern-Generating Circuits," *Annual Review of Neuroscience*, vol. 31, pp. 271–294, July 2008.

[57] G. J. Gutierrez, T. O'Leary, and E. Marder, "Multiple Mechanisms Switch an Electrically Coupled, Synaptically Inhibited Neuron between Competing Rhythmic Oscillators," *Neuron*, vol. 77, pp. 845–858, Mar. 2013.

[58] A. J. Ijspeert and M. A. Daley, "Integration of feedforward and feedback control in the neuromechanics of vertebrate locomotion: a review of experimental, simulation and robotic studies," *Journal of Experimental Biology*, vol. 226, p. jeb245784, Aug. 2023.

[59] V. Lobato-Rios, S. T. Ramalingasetty, P. G. Özdil, J. Arreguit, A. J. Ijspeert, and P. Ramdya, "NeuroMechFly, a neuromechanical model of adult Drosophila melanogaster," *Nature Methods*, vol. 19, pp. 620–627, May 2022.

[60] R. Vaxenburg, I. Siwanowicz, J. Merel, A. A. Robie, C. Morrow, G. Novati, Z. Stefanidi, G.-J. Both, G. M. Card, M. B. Reiser, M. M. Botvinick, K. M. Branson, Y. Tassa, and S. C. Turaga, "Whole-body physics simulation of fruit fly locomotion," *Nature*, pp. 1–9, Apr. 2025.

[61] J. Braun, F. Hurtak, S. Wang-Chen, and P. Ramdya, "Descending networks transform command signals into population motor control," *Nature*, vol. 630, no. 8017, pp. 686–694, 2024.

[62] A. S. Bates, J. S. Phelps, M. Kim, H. H. Yang, A. Matsliah, Z. Ajabi, E. Perlman, K. M. Delgado, M. A. M. Osman, C. K. Salmon, J. Gager, B. Silverman, S. Renauld, M. F. Collie, J. Fan, D. A. Pacheco, Y. Zhao, J. Patel, W. Zhang, L. Serratosa Capdevilla, R. J. Roberts, E. J. Munnelly, N. Griggs, H. Langley, B. Moya-Llamas, R. T. Maloney, S.-c. Yu, A. R. Sterling, M. Sorek, K. Kruk, N. Serafetinidis, S. Dhawan, T. Stürner, F. Klemm, P. Brooks, E. Lesser, J. M. Jones, S. E. Pierce-Lundgren, S.-Y. Lee, Y. Luo, A. P. Cook, T. H. McKim, E. C. Kophs, T. Falt, A. M. Negrón Morales, A. Burke, J. Hebditch, K. P. Willie, R. Willie, S. Popovych, N. Kemnitz, D. Ih, K. Lee, R. Lu, A. Halageri, J. A. Bae, B. Jourdan, G. Schwartzman, D. D. Demarest, E. Behnke, D. Bland, A. Kristiansen, J. Skelton, T. Stocks, D. Garner, F. Salman, K. C. Daly, A. Hernandez, S. Kumar, T. B.-F. Consortium, S. Dorkenwald, F. Collman, M. P. Suver, L. M. Fenk, M. J. Pankratz, G. S. Jefferis, K. Eichler, A. M. Seeds, S. Hampel, S. Agrawal, M. Zandawala, T. Macrina, D.-Y. Adjavon, J. Funke, J. C. Tuthill, A. Azevedo, H. S. Seung, B. L. de Bivort, M. Murthy, J. Drugowitsch, R. I. Wilson, and W.-C. A. Lee, "Distributed control circuits across a brain-and-cord connectome," *bioRxiv*, 2025.

[63] S. Amari, *Mathematics of Neural Networks (in Japanese)*. 1978.

[64] A. C. E. Onslow, M. W. Jones, and R. Bogacz, "A Canonical Circuit for Generating Phase-Amplitude Coupling," *PLOS ONE*, vol. 9, p. e102591, Aug. 2014.

[65] J. L. Alvarez, K. Morrison, and C. Curto, "Attractor-based models for sequences and pattern generation in neural circuits," June 2025.

[66] F. D. Wandler, B. K. Lemberger, D. L. McLean, and J. M. Murray, "Coordinated spinal locomotor network dynamics emerge from cell-type-specific connectivity patterns," *eLife*, vol. 14, June 2025.

[67] V. Dvornyk, O. Vinogradova, and E. Nevo, "Origin and evolution of circadian clock genes in prokaryotes," *Proceedings of the National Academy of Sciences*, vol. 100, pp. 2495–2500, Mar. 2003.

[68] M. B. Elowitz and S. Leibler, "A synthetic oscillatory network of transcriptional regulators," *Nature*, vol. 403, pp. 335–338, Jan. 2000.

[69] J. Stricker, S. Cookson, M. R. Bennett, W. H. Mather, L. S. Tsimring, and J. Hasty, "A fast, robust and tunable synthetic gene oscillator," *Nature*, vol. 456, pp. 516–519, Nov. 2008.

[70] E. Marder, S. Kedia, and E. O. Morozova, "New insights from small rhythmic circuits," *Current Opinion in Neurobiology*, vol. 76, p. 102610, 2022.

[71] D. Aldarondo, J. Merel, J. D. Marshall, L. Hasenclever, U. Klibaite, A. Gellis, Y. Tassa, G. Wayne, M. Botvinick, and B. P. Ölveczky, "A virtual rodent predicts the structure of neural activity across behaviours," *Nature*, vol. 632, pp. 594–602, Aug. 2024.

[72] S. Dorkenwald, C. M. Schneider-Mizell, D. Brittain, A. Halageri, C. Jordan, N. Kemnitz, M. A. Castro, W. Silversmith, J. Maitin-Shephard, J. Troidl, *et al.*, "Cave: Connectome annotation versioning engine," *Nature Methods*, pp. 1–9, 2025.

[73] P. Dayan and L. F. Abbott, *Theoretical neuroscience: computational and mathematical modeling of neural systems*. MIT press, 2005.

[74] C. M. Schneider-Mizell, S. Gerhard, M. Longair, T. Kazimiers, F. Li, M. F. Zwart, A. Champion, F. M. Midgley, R. D. Fetter, S. Saalfeld, and A. Cardona, "Quantitative neuroanatomy for connectomics in *Drosophila*," *eLife*, vol. 5, p. e12059, mar 2016.

[75] J. Bradbury, R. Frostig, P. Hawkins, M. J. Johnson, C. Leary, D. Maclaurin, G. Necula, A. Paszke, J. VanderPlas, S. Wanderman-Milne, and Q. Zhang, "JAX: composable transformations of Python+NumPy programs," 2018.

[76] P. Kidger, "On neural differential equations," *arXiv preprint arXiv:2202.02435*, 2022.

[77] A. Mathis, P. Mamidanna, K. M. Cury, T. Abe, V. N. Murthy, M. W. Mathis, and M. Bethge, "Deeplabcut: markerless pose estimation of user-defined body parts with deep learning," *Nature Neuroscience*, 2018.

[78] P. Karashchuk, K. L. Rupp, E. S. Dickinson, S. Walling-Bell, E. Sanders, E. Azim, B. W. Brunton, and J. C. Tuthill, "Anipose: A toolkit for robust markerless 3d pose estimation," *Cell Reports*, 2021.

[79] R. J. Moore, G. J. Taylor, A. C. Paulk, T. Pearson, B. v. Swinderen, and M. V. Srinivasan, "Fictrac: A visual method for tracking spherical motion and generating fictive animal paths," *Journal of Neuroscience Methods*, 2014.

Methods

VNC connectome datasets: MANC and FANC

Our VNC connectome simulations were constructed based on two published datasets, the male (MANC, [27]) and female (FANC, [28]) adult nerve cord connectome datasets. Unless stated otherwise, simulation results throughout the manuscript are from the MANC dataset, because it is more comprehensively proofread. To select a subset of cells to simulate from the entire MANC dataset, we first selected all front leg motor neurons (class "motor neuron", subclass "fl"). Next we added all front leg premotor neurons by querying for any neuron that made synaptic outputs onto any of those leg motor neurons. Finally, we added all descending neurons (class "descending neuron") that made any synaptic outputs onto the front leg premotor neurons. After collecting this initial set of neuron IDs, we filtered for neurons that were proofread and had been assigned a neurotransmitter prediction. In this way, we constructed the front leg motor network $\mathbf{W}$ (as illustrated in **Fig. 1b**), defined as the set of recurrent connections between any nodes in this set. Each element $|w_{ij}|$ was the number of synapses detected from neuron j to neuron i. To remove very weak connections and a small number of neurons that made only very weak connections to this network, we imposed a floor of 5 synapses. The sign of w_{ij} was assigned to be positive if the presynaptic neuron j was predicted to be cholinergic and negative if neuron j was predicted to be GABAergic or glutamatergic (according to the "predictedNt" property).

In the FANC connectome simulations, we applied an analogous set of criteria to construct $\mathbf{W}$. We restricted the network to the left front leg because this neuropil is the most thoroughly proofread and annotated [28, 30]. We started with front left leg motor neurons (from motor_neuron_table_v7 CAVE annotation table), then added local premotor neurons (i.e., those with neurites constrained to the front left leg neuropil, from left_t1_local_premotor_table_v6), and the single descending neuron DNg100. As in MANC, the network consisted of all recurrent connections among these neurons, with $|w_{ij}|$ being synapse counts. Unlike the MANC dataset, the FANC dataset does not have an automated classifier to predict the neurotransmitter for each neuron. However, the developmental hemlineage of neurons with somas within the VNC can be determined anatomically and is highly predictive of the neurotransmitter released by each neuron [30]. Therefore, we used the hemilineage annotations from the corresponding CAVE tables[72] to assign a positive or negative sign to each cell's output. The only exceptions to this approach were made because of a set of discrepancies we noticed between the FANC and MANC datasets in hemilineage assignments. Specifically, 4 neurons (segIDs 72905112552773752, 72975481296715415, 72975481363813393, 72905112552782067) are grouped with glutamatergic hemilineages in FANC so would be considered inhibitory, but the same cells in MANC (bodyIDs 162543, 11751, 13246, 15115) have an indeterminate hemilineage assignment of "TBD". In MANC, an independent neurotransmitter classifier predicted that all 4 of these neurons are cholingergic (with probability > 0.81), so they would be excitatory. Taken together, we reasoned that since there is no agreement on hemilineage assignments and high probability scores from the MANC neurotransmitter prediction, so these four cells are more likely excitatory. Therefore, we assigned their output synapse weights to be positive.

Connectome simulation models

We developed a firing rate model to simulate the activity (rate $r(t)$ in Hz) of every cell in the network as a function of its synaptic connectivity and external inputs $I(t)$ (**Equation 1**). The form of this equation follows a standard formulation of a firing rate model [73]. Each cell had four biophysical parameters; below, we elaborate on how these parameters were randomly chosen for each replicate of the simulation.

We chose the input nonlinearity to be a positive-rectified hyperbolic tangent function $[\tanh(x)]_+$, where $[x]_+$ denotes $\max(x, 0)$. The function was parameterized as $f(x) = [r^{\max} \tanh(\frac{a}{r^{\max}} x - \theta)]_+$ so that parameters have straightforward interpretations. In particular, $r^{\max}$ is the upper bound, θ is the minimal input needed to produce a nonzero output, and a is the slope at this threshold value ($a = \lim_{x \to \theta+} \frac{df}{dx}$) (**Fig. 1d**).

Although this nonlinearity has an upper bound $r^{\max}$, in most of the rhythm-generating simulation results presented in this paper, the firing rates stayed well within the approximately linear regime, so that the neural dynamics could have been effectively captured by a simpler nonlinearity (e.g. ReLU). However, we chose the rectified tanh function because some simulations led to oversaturated or unstable output (e.g., in some DN activation screens and noise perturbation shuffles), so that capping firing rates supported more stable numerical solutions.

Biophysical parameter distributions

For each cell and in each random replicate of the simulation, we drew its biophysical parameters from normal distributions truncated at zero, then normalized two of the parameters by neuron size (as elaborated below). Across all simulations, the gain (before size normalization) was $a^* \sim \mathcal{N}(1, 0.1)$, the threshold (before size normalization) was $\theta^* \sim \mathcal{N}(7.5, 0.6)$, the max firing rate was $r^{\max} \sim \mathcal{N}(200, 10)$ Hz, and the time constant was $\tau \sim \mathcal{N}(0.02, 0.002)$ sec. Next, a_i^* was divided by the median-normalized size of each neuron i, and θ_i^* was multiplied by the median-normalized size of each neuron i, resulting in distributions for a and θ with long tails (**Fig. 1d**).

Our choice of these parameter distributions was based on a combination of physiologically feasible ranges reported in the literature and a hyperparameter search. Since $r^{\max}$ and τ have direct biological interpretations, we used reasonable ranges for firing rate limits and time constants, respectively, of *Drosophila* neurons given experimental literature [44, 42] and consistency with previous fly neuron simulation studies [45, 35]. In our model, gain was dimensionless and units of input were arbitrary, since voltage was not directly modeled. Therefore, values of θ and a have no direct biological analogs. In our hyperparameter search, we evaluated a grid of values for the four biophysical parameters as well as the synaptic scaling constant b on a set of simple monosynaptic connections. In this test network, we chose ranges of values that produced consistent activity in downstream neurons when stimulated with input, but this activity also decayed to quiescence after input was removed.

To normalize θ and a by neuron size s_i, we used morphological data from FANC and MANC. For each cell, a^* and θ^* were randomly drawn from the distributions described above, then gain was divided by s_i and threshold was multiplied by s_i. In MANC, we used the available volume property. In FANC, we accessed the neuron meshes in the reconstruction to calculate the surface area of each cell. In both datasets, we took the ratio of each cell's size to the median cell size in the dataset as the value used to scale gain and threshold. We reasoned that, in most neurons, a significant amount of cell volume is accounted for by the approximately cylindrical neurites, so that volume is approximately linearly related to surface area, which is the determining factor for input resistance. This approach allowed us to account for the general differences in excitability between large and small neurons, and this consideration was critical in our simulation results. Other connectome analyses have normalized the strength of synaptic connections by the total number of synaptic inputs received by the postsynaptic cell [74], which is similar to size normalization, since large neurons tend to receive many synapses.

Implementation of numerical simulations

To compute solutions to the firing rate models of our connectome simulations, we implemented a numerical differential equation solver using the GPU-accelerated numerical computing library JAX [75]. Our solver used Diffrax [76] with the Runge-Kutta integration method of order 5(4) (`diffrax.Dopri5()`). Error tolerances were chosen to be `rtol=2e-6` and `atol=5e-9`, based on hyperparameter searches of values that minimized both runtime and sum-squared error when compared to a reference run with very small error tolerances. Run on 4 Nvidia L40s GPUs, 1024 replicates of the DNg100 activation in the full front leg MANC model typically ran in ∼18 minutes.

Leaky integrate-and-fire model

To confirm that the rhythm generating behavior of the core CPG circuit does not depend on our specific firing-rate model formulation, we simulated the dynamics of the same connectome weights using a spiking neuron model. We implemented a leaky integrate-and-fire (LIF) model based on the same parameter values from previous work [35], without fine tuning or training. Specifically, we used the following parameters: $V_{\text{rest}} = -52$ mV, $V_{\text{reset}} = -52$ mV, $V_{\text{thresh}} = -45$ mV, $t_{\text{refractory}} = 2.2$ ms, $\tau_{\text{membrane}} = 20$ ms, $\tau_{\text{synaptic}} = 5$ ms, $w_{\text{synaptic}} = 0.275$ mV, $t_{\text{delay}} = 1.8$ ms, $V_{\text{init}} = -52$ mV, $dt = 0.01$ ms, simulation time = 3 s, network input = 0.15 nA. The membrane time constant was not specifically mentioned in [35], so we computed it based on the membrane resistance $R_m = 10$ kΩ cm^2 and membrane capacitance $C_m = 2$ μF cm^{-2} values reported to arrive at $\tau_{\text{membrane}} = R_m C_m$.

Linearized dynamical system analysis

We performed an eigendecomposition of the linearized dynamical system corresponding to the full MANC network and the minimal circuit (core CPG circuit and DNg100) to confirm the oscillatory behavior and oscillation frequencies observed in simulations. For this analysis, we simplified the dynamical system equation to $\tau \frac{\mathrm{d}\mathbf{h}}{\mathrm{d}t} = -\mathbf{h} + \phi(\mathbf{W}\mathbf{h} + I)$, then discretized and linearized it to $\mathbf{h}_{t+\mathrm{d}t} = (1 - \alpha + \alpha g \mathbf{W})\mathbf{h}_t + \alpha g I$, where $\alpha = \mathrm{d}t/\tau$, and g is the non-linearity gain at time t, which is potentially different for each neuron (column-wise multiplication with $\mathbf{W}$, element-wise multiplication with I). With $\mathbf{W}^* \equiv 1 - \alpha + \alpha g \mathbf{W}$, we decomposed the dynamics matrix by eigendecomposition and denoted vectors expressed in the eigenbasis by a hat $\widehat{\cdot}$. In this basis, we find $\widehat{\mathbf{h}_{t+\mathrm{d}t}} = \mathbf{D}^* \widehat{\mathbf{h}_t} + \alpha g \widehat{I}$, where $\mathbf{D}^*$ is the diagonal form of $\mathbf{W}^*$ with eigenvalues $\lambda^* = 1 - \alpha + \alpha g \lambda$.

The system is oscillatory if it has pairs of complex-conjugate eigenvalues. We simplified the solution to find the oscillation frequency of the system. We let $\lambda^* \equiv a^* + \mathrm{i}b^* \equiv r^* e^{\mathrm{i}\theta^*}$, where $\theta^* = \mathrm{atan2}(b^*, a^*)$. Thus, we found $\widehat{h_{k,i}} \sim r^{*k+1} e^{\mathrm{i}(k-1)\theta^*} - r^* e^{-\mathrm{i}\theta^*} - r^{*k} e^{\mathrm{i}k\theta^*} + 1$. We computed the oscillation frequency according to $f = 1/(\Delta k \mathrm{d}t)$, where we chose Δk such that $\widehat{h_{k,i}}$ and $\widehat{h_{k+\Delta k,i}}$ have the same phase. With $\alpha \ll 1$, then $r^* \approx 1$, and we found $\Delta k \approx 2\pi/\theta^*$, and finally $f = \frac{\mathrm{atan2}(\alpha g b, 1-\alpha+\alpha g a)}{2\pi \mathrm{d}t}$.

To analyze the network dynamics matrix $\mathbf{W}$ and the core CPG network, we scaled each neuron's gain according to its size (as described above in Biophysical parameter distributions), then multiped by an overall gain factor of 0.75 to approximate the simulated nonlinearity (scaled tanh function). Calculations used an average time constant of $\tau = 20$ ms and a timestep $\mathrm{d}t = 0.01$ ms. For the minimal CPG network, the eigenvalues of $\mathbf{W}^*$ were $\{0.9908 + 0.0879j, 0.9908 - 0.0879j, 0.8683, 0.95\}$, confirming the oscillatory nature of the system with an oscillation frequency of approximately 14 Hz.

Motor rhythmicity score

To quantify the degree to which circuit simulations generated rhythmic activity patterns in leg motor neurons, we developed a *motor rhythmicity score* that was used throughout the paper to evaluate and screen circuit models. Our goal was to devise a simple metric, based on autocorrelations, with the property that repeating signals would receive high scores even if they were not necessarily symmetric waveforms (e.g., both a sine wave and a sawtooth would receive a high score).

The motor rhythmicity score assigned to each simulation was computed as the average of rhythmicity scores for all active motor neurons. A motor neuron was included if its $r_i(t) > 0.01$ at any time after $t = 250$ ms. To compute a motor neuron's rhythmicity score, we take the trace of its activity after the initial transient response until the end of the simulation (250 ms to end). This trace was normalized so that it is between -1 and 1, $\hat{r}(t) = 2\frac{r(t) - \min(r)}{\max(r)} - 1$. We then computed the autocorrelation of $\hat{r}$ and detected peaks in this autocorrelation, with a prominence threshold of 0.05. The "raw score" for this neuron was assigned as the smaller of the maximum peak height (magnitude above zero) and the maximum peak prominence (magnitude between peak and valley). Using the time shift Δt value at which the most prominent peak occurred as the period of the dominant rhythm, we then computed the same score for a

reference sinusoidal waveform with the same frequency and total duration. To normalize the rhythmicity score between 0 and 1, we divided the raw score by the reference score of this frequency-matched sinusoidal signal. Examples of individual motor neuron traces with their scores are shown in **Fig. 1e**. If a motor neuron is active, but there is no prominent peak in the autocorrelation, the neuron received a score of 0.

Kinematic rhythmicity score

To quantify the degree to which leg joint kinematics were rhythmic in DNb08 activation experiments **Fig. 4e**, we used the same calculation as the motor rhythmicity score to evaluate individual joint angle traces. We used the joint angle during a 2 second time window, beginning 0.5 seconds after stimulus onset. Traces for which the detected peak frequency was slower than 1 Hz were assigned a score of 0.

Descending neuron activation screen

We conducted a computational screen in which each of the 933 putative excitatory descending neurons (DNs) in our model was stimulated with a tonic input, and we assessed how much motor neuron outputs driven by that DN was rhythmic (as quantified by the motor rhythmicity score). We conducted this activation screen in a network constructed from MANC because this dataset included neurotransmitter predictions of all DNs; our FANC network was used to investigate the DNg100 circuit specifically and only contains that descending neuron. Each simulation replicate was 1 second in duration, with the tonic input stimulus onset at 20 ms. Because the input strength I_{stim} was arbitrary in magnitude in our model, we automatically tuned I_{stim} over a range of values depending on if the simulation was underactive or oversaturated. Underactive simulations were defined as having fewer than 5 neurons recruited in the whole network, and oversaturated simulations were defined as having more than 500 neurons recruited, because such simulations were generally unstable. If the simulation was underactive, I_{stim} was doubled, or set to the midpoint to the next highest value that had been tried. If it was oversaturated, I_{stim} was halved, or set to the midpoint to the next lowest value that had been tried. In each replicate, this automated adjustment was repeated up to a maximum of 10 times to try to achieve a reasonable stimulus strength. If after these 10 iterations, the simulation was still underactive or oversaturated, it was consider infeasible and the motor rhythmicity score for this replicate was not computed (set to NaN). Out of the 933 neurons screened, 749 (80.3%) had at least one feasible replicate out of 16, and 694 (74.4%) had at least 5 feasible replicates. Reported motor rhythmicity scores for each neuron (**Fig. 1e**, **Supplementary Table 1 and 6**) were the mean score of the feasible replicates.

Computational sufficiency screen with iterative pruning

We developed an iterative procedure to isolate a subset of cells in the full network that were sufficient to generate rhythmic motor patterns in a reduced model (illustrated in **Fig. 3b**). We started with a full intact network and one random seed for the biophysical parameters of its cells (these parameters were frozen for all iterations in one pruning procedure). As in the DN activation screen, simulations were 1 second in duration and consisted of a tonic input to a single descending neuron with an onset at 20 ms. For DNg100 activation, $I_{\text{stim}} = 250$ in MANC and 150 in FANC (these activations have arbitrary units and were set by the procedure described in the activation screen). For DNb08 activation, $I_{\text{stim}} = 65$. Leg motor neurons were not considered by the pruning screen, so they all remain present in all simulated networks.

Each replicate of the computational sufficiency screen executed the following stochastic procedure to prune neurons from the model network, until convergence to a minimal network according to the stopping criterion. First, all neurons that were not active were pruned from the network. Thereafter, at each step, one additional neuron was chosen to be silenced, with a probability inversely proportional to its maximum firing rate at the last iteration. We then simulated DN activation of this new network and evaluated its motor rhythmicity score. If the motor rhythmicity score of this pruned network still exceeded a threshold value (≥ 0.5), this silenced neuron, along with any inactive neurons, were permanently pruned

in the next iteration. If the motor rhythmicity score of a pruned network fell below the threshold, then it was returned to the network. This procedure was then repeated by choosing another neuron to silence. Finally, the stopping criterion was when no neuron in the pruned network could be removed without producing a motor rhythmicity score below threshold, at which point we considered the pruning screen to have converged. The remaining cells in the network formed a sub-circuit (with the DN input, recurrent network of interneurons, and all motor neuron outputs) that was sufficient to generate rhythmic activity, in the sense that they were computationally isolated from the initial full network simulation. Because the biophysical parameters and the choices of neurons to silence were stochastic, we repeated the screen 1024 times for each full network (MANC and FANC) activated by each DN (DNg100 and DNb08).

Fly behavior and optogenetics experiments

Genotypes used

Name	**Genotype**	**Figures**
DNg100>CsChrimson	w[1118]/w[1118]; VT058557-GAL4.AD/+; R85F12-GAL4.DBD/20xUAS-CsChrimson-tdTomato su(Hw)attP1	**2h,i,j S2**
SS70620>CsChrimson	w[1118]/w[1118]; P{y[+t7.7] w[+mC]=R94D12-p65.AD}attP40/+; P{y[+t7.7] w[+mC]=VT031392-GAL4.DBD}attP2/20xUAS-CsChrimson-tdTomato su(Hw)attP1	**4d,e**

Optogenetics experiments with 3D joint kinematics

Methods for behavioral experiments were previously described in [42]. Briefly, female flies were cold-anesthetized, de-winged, decapitated, and tethered (0.1 mm tungsten rod) with UV glue (KOA 300). For DNg100 experiments, we used flies that were 10–12 days old, as in [47], because this produced more robust walking behavior, possibly due to accumulated CsChrimson expression. For DNb08 experiments, we used flies that were 2–5 days old. Each fly recovered for 10–15 minutes before being positioned in the behavioral arena. For DNg100 experiments, flies were postioned on an air-supported spherical treadmill (0.13 g, 9.08mm diameter). To activate DNs, a LED laser (638 nm, 1200 Hz, 30% duty cycle, Laserland) was focused at the body-coxa joint of the front left leg. Each trial consisted of 5 seconds pre-stim, 5 seconds stim-on, and 5 seconds post-stim, for a total trial length of 15 seconds. Trials were run in blocks of 12: 8 experimental trials with the LED laser stimulus on and 4 control trials where the stimulus was off. We recorded each trial using 6 high-speed cameras (300 fps; Basler acA800–510 µm; Balser AG) and tracked 3D leg joint kinematics using DeepLabCut [77] and Anipose [78]. The movements of the ball were recorded with a FLIR camera (FMVU-03MTM-CS, 30 FPS) and processed with FicTrac [79] to read out the forward velocity of the fly. We used a custom Python script to analyze kinematics based on the Anipose tracking data. Stepping frequency was computed on the tracked tarsus tip position along the anterior-posterior axis of the fly during the stimulus period. The frequency of each trial was calculated as the inverse of the average time between peaks, which was detected with `scipy.signal.find_peaks` using a minimum prominence of 0.15 and a minimal temporal distance of 50 ms.

To test DNg100 modulation of walking speed in headless flies, we used laser intensities of 0.03, 0.09, and 0.33 mW/mm^2 (8 experimental trials of each intensity per fly). DNg100 activation produced forward walking on the ball, but at a lower speed than is typical of wild-type flies [50]. They generally exhibited a tetrapod coordination pattern (**Supplementary Fig. 2**).

Supplementary Materials

Supplementary Video 1: Optogenetic activation of DNg100 neurons drives walking in headless flies. Corresponds to experimental data in **Fig. 2i–k**.

Supplementary Video 2: Optogenetic activation of DNb08 neurons drives oscillatory leg movements in headless flies. Corresponds to experimental data in **Fig. 4d–e**.

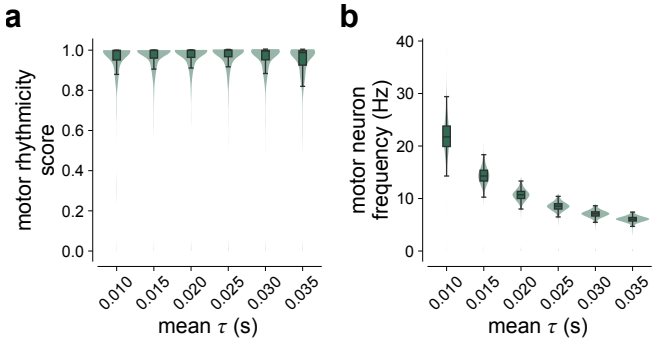

Supplementary Figure 1: Time constant (τ) vs. motor neuron frequency. **a**, Adjusting the mean τ in parameter distributions did not affect the distribution of motor rhythmicity scores. **b**, The frequency of the motor neuron oscillations is inversely proportional to the mean τ value.

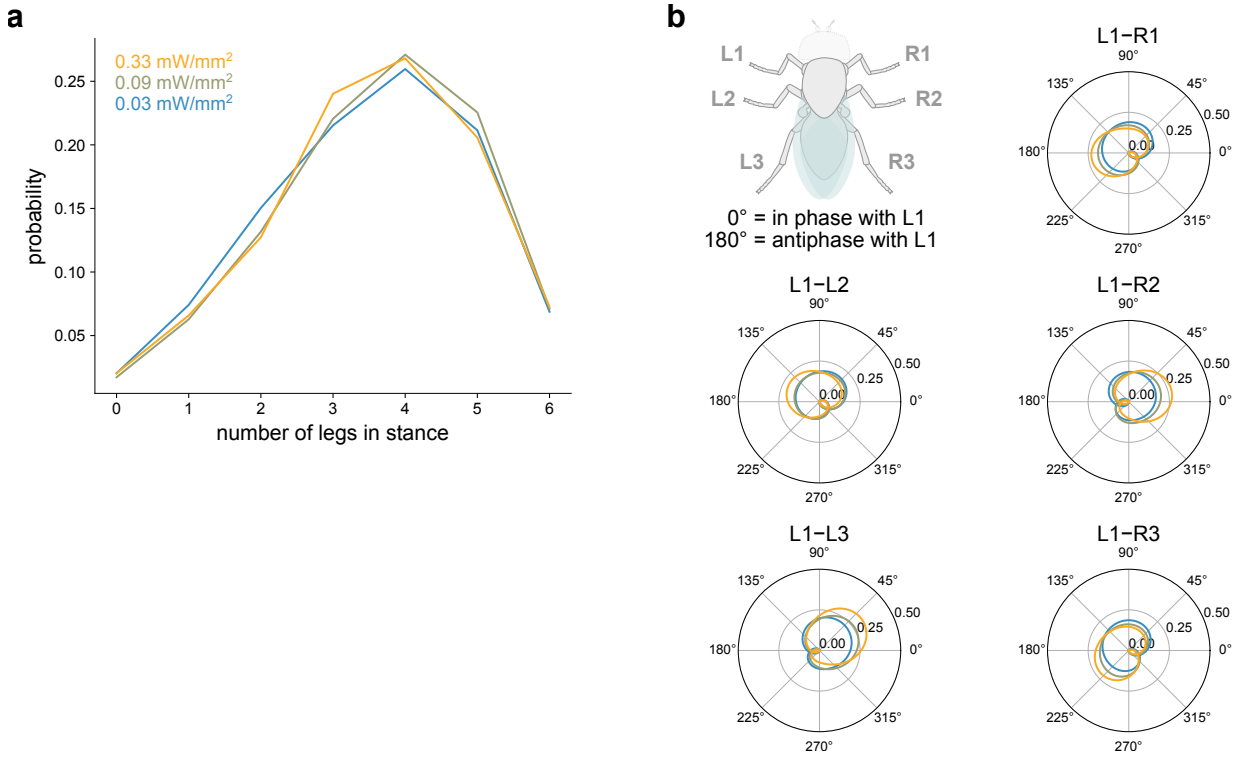

Supplementary Figure 2: Interleg coordination patterns during optogenetic DNg100 activation in headless flies. **a**, Probability of n legs being in stance simultaneously during DNg100-driven walking, with n from 0 to all 6 legs, at each laser intensity. **b**, Relative phase between legs at each laser intensity.

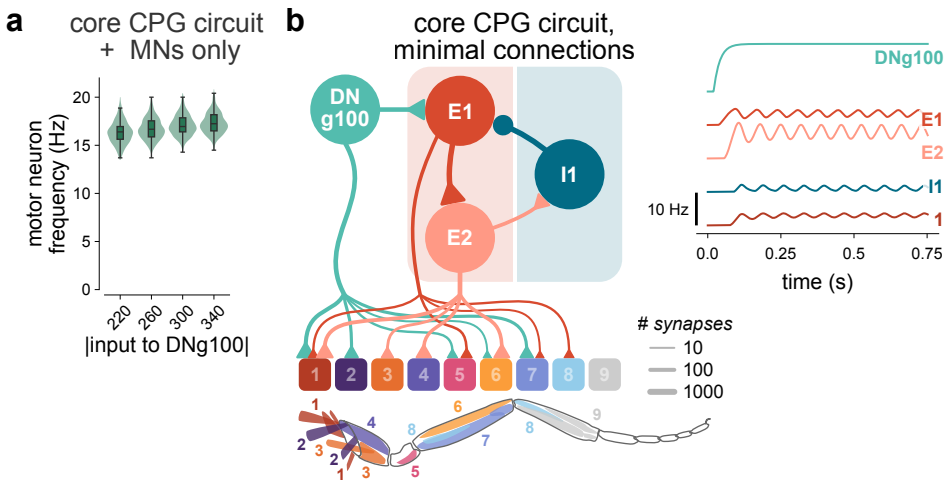

Supplementary Figure 3: Additional properties of the core CPG circuit. a, The core CPG circuit does not show the same modulation of motor neuron frequency with DNg100 input strength as the full network does (n=512 replicates per condition). Simulations with no active motor neurons were omitted. Green shaded regions are distributions of frequencies, and black bars indicate medians and quartiles. **b,** Core CPG circuit in which all interneuron-interneuron connections aside from the cyclic E1 → E2 → I1 → E1 connections have been removed still produces rhythmic activity.

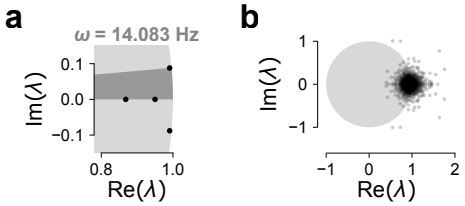

Supplementary Figure 4: Eigenvalue spectra of linearized dynamical systems corresponding to reduced and full circuits. a, Eigenvalues of the linearized dynamical system of the 4-neuron subcircuit consisting of only the left DNg100, E1 L, E2 L, and I1 L. The light gray region denotes the unit circle in the complex plane. The pair of complex-valued eigenvalues corresponds to an oscillation frequency of about 14 Hz. **b**, Eigenvalues of the linearized dynamical system of the full MANC front leg motor network.

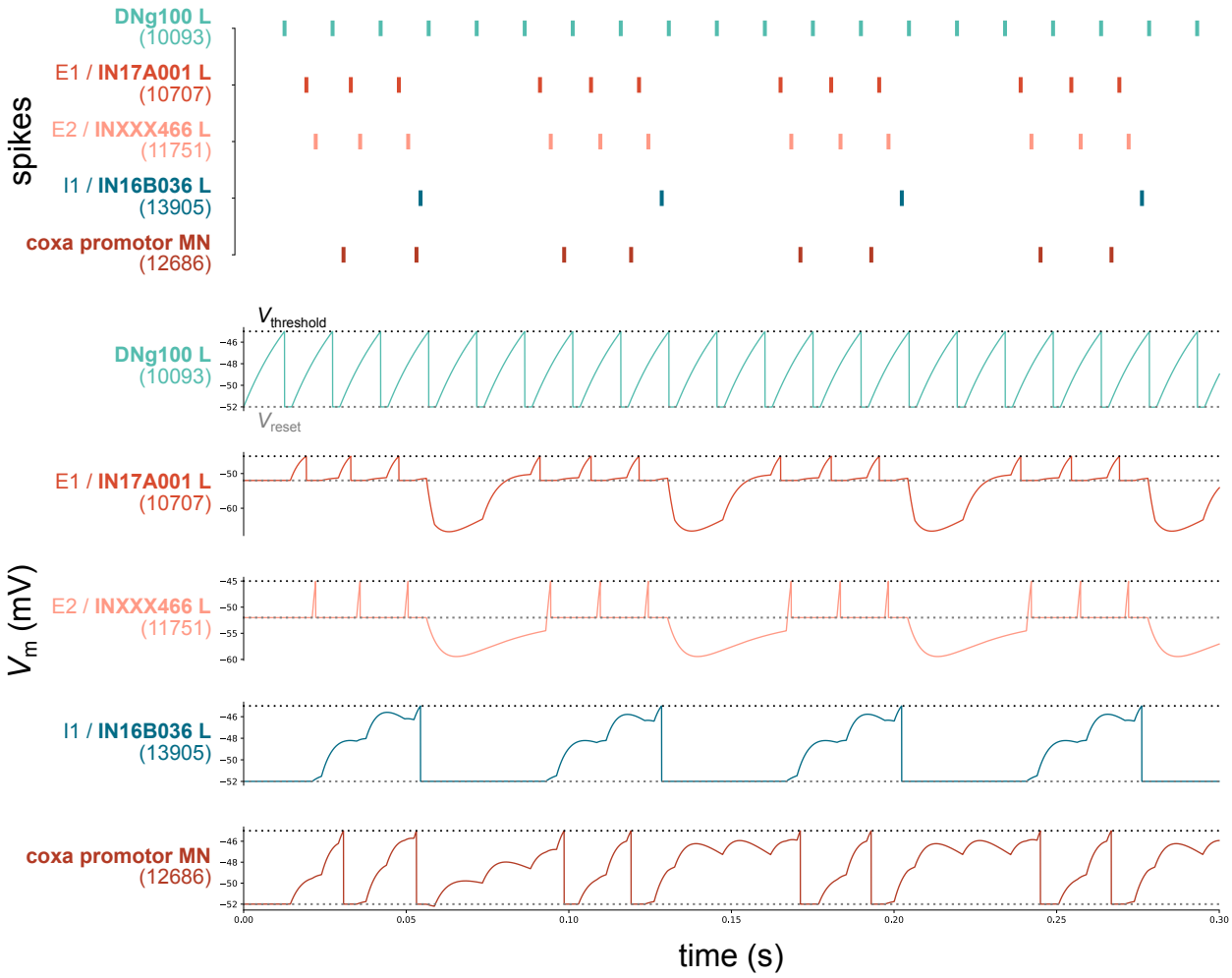

Supplementary Figure 5: Leaky integrate-and-fire model of core CPG circuit showed rhythmic activity. Simulation included a subcircuit consisting of only the left DNg100, E1 L, E2 L, I1 L, and all of leg motor neurons. *Top*: Spike times, and *Bottom*: voltage (V_m) for each of the core CPG neurons, and one motor neuron.

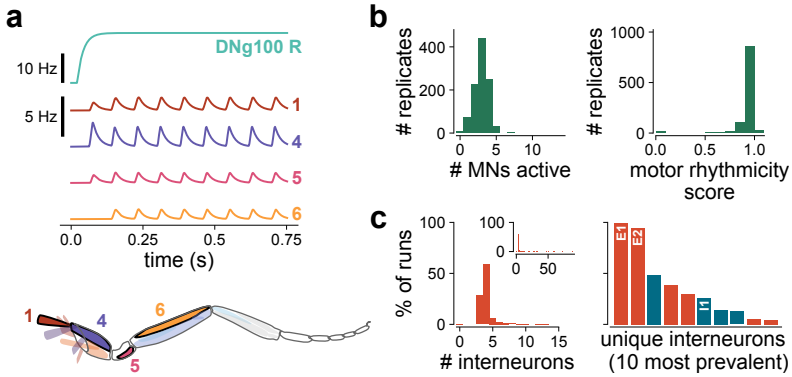

Supplementary Figure 6: DNg100 R activation. **a**, Example activity of MANC network with step DNg100 R stimulation. Selected motor neurons shown, with numbers corresponding to muscles innervated in the anatomical diagram. **b**, DNg100 R activation consistently produces motor rhythms (n=1000 replicates). **c**, Circuits identified by pruning (n=297 replicates, right DNg100, MANC). *Left*: Number of interneurons that are in minimal circuits (one outlier of 30 neurons not shown). *Right*: Percentage of simulation runs in which minimal circuits contained unique interneurons.

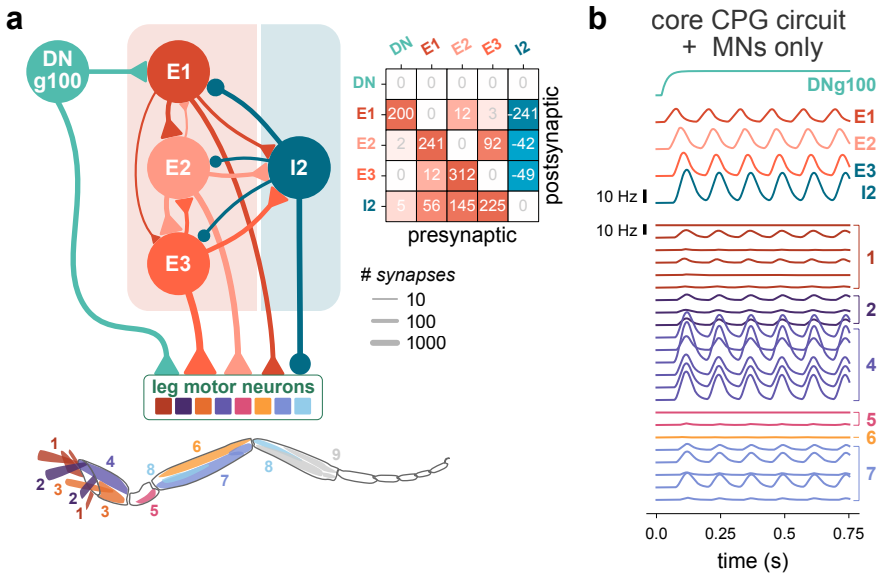

Supplementary Figure 7: FANC core CPG circuit. a, The most common minimal circuit in FANC and its connectivity to motor neurons (shown are connections of at least 10 synapses). Triangles and circles are excitatory and inhibitory connections, respectively. Synapse counts are summed across all leg motor neurons. Inset shows weight matrix. **b,** Example activity of the isolated four-neuron circuit.

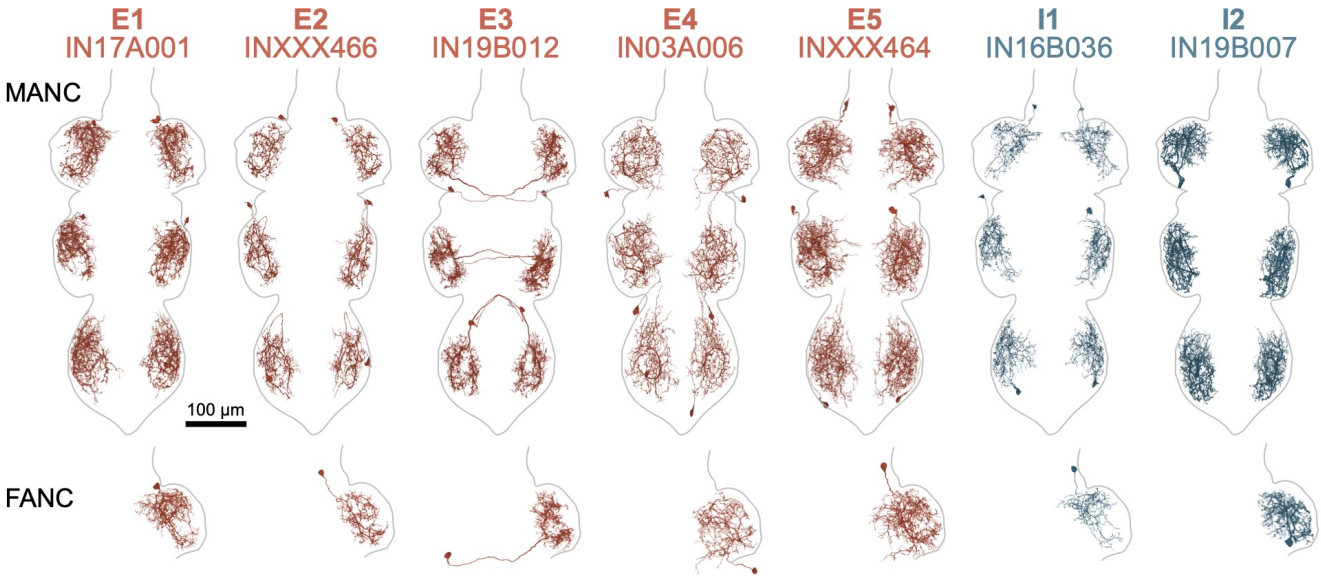

Supplementary Figure 8: Morphologies of VNC interneurons identified in the computational sufficiency screens. Cell type correspond to the most commonly identified cells in **Supplementary Tables 2, 3, and 4**. *Top:* All neurons of each type in MANC. Each of these cell types consists of exactly one neuron per leg neuropil. *Bottom:* The neuron of the same type identified in the FANC front left leg neuropil.

bodyId	type	mean motor rhythmicity score
10339	DNg100	0.983424
10093	DNg100	0.978602
14061	DNb08	0.955253
30919	DNg12	0.905598
18279	DNp41	0.865838
16683	DNxl091	0.860995
18153	DNp41	0.847139
14966	DNb08	0.841571
13892	DNb08	0.839170
32815	DNg12	0.813234
14680	DNb08	0.801999
25931	DNa07	0.786021
12221	DNxl121	0.766589
44321	DNit011	0.764497
23461	DNfl031	0.735547
17031	DNxl092	0.731611
15841	DNp71	0.714360
19821	DNg54	0.687533
32742	DNg12	0.668965
38587	DNg12	0.647725
37139	DNit013	0.646784
30130	DNxn167	0.636139
11164	DNa13	0.625670
26047	DNg09	0.624473
11145	DNa13	0.620487
16264	DNxn159	0.603845
10291	DNxl134	0.586567
25645	DNut054	0.584007
23962	DNxn127	0.567792
10896	DNxl133	0.566917
11981	DNp43	0.551802
22194	DNxn171	0.546201
27523	DNfl025	0.523922
27095	DNfl025	0.521211
13257	DNxl103	0.512680
12791	DNxl110	0.508832
11311	DNa13	0.500819

Supplementary Table 1: Top scoring neurons in descending neuron activation screen. All descending neurons with a mean motor rhythmicity score >0.5, corresponding to **Fig. 1e**.

bodyIds	types	count
10707, 11751, 13905	IN17A001 (E1), INXXX466 (E2), IN16B036 (I1)	636
10707, 10715, 11751, 12026, 17664	IN17A001 (E1), IN19B012 (E3), INXXX466 (E2), IN13A010 (–), MNfl10 (–)	123
10242, 10707, 11751	IN19A007 (I2), IN17A001 (E1), INXXX466 (E2)	102
10707, 10715, 11751, 12026	IN17A001 (E1), IN19B012 (E3), INXXX466 (E2), IN13A010 (–)	33
10707, 11751, 11799, 17664, 162543	IN17A001 (E1), INXXX466 (E2), IN19A020 (–), MNfl10 (–), INXXX464 (E5)	11

Supplementary Table 2: Converged minimal circuits for DNg100 pruning screen in MANC. All distinct sets of interneurons that appeared at least 10 times out of 1024 pruning screens.

segIds	types	count
72483380721505294, 72834674820722635, 72975481296715415, 73820799177797612	IN19A007 (I2), IN17A001 (E1), INXXX466 (E2), IN19B012 (E3)	721
72483380721505294, 72834674820722635, 72905112552773752, 72975481296715415	IN19A007 (I2), IN17A001 (E1), INXXX464 (E5), INXXX466 (E2)	89
72694075576809644, 72834674820722635, 72975481296715415, 73820799177797612	IN13A010 (–), IN17A001 (E1), INXXX466 (E2), IN19B012 (E3)	36
72483380721505294, 72834674820722635, 72905112552773752, 72975481296715415, 72975481364113281	IN19A007 (I2), IN17A001 (E1), INXXX464 (E5), INXXX466 (E2), 8A (–)	25
72834674820722635, 72905112619913957, 72975481296715415, 73820799177797612	IN17A001 (E1), IN16B036 (I1), INXXX466 (E2), IN19B012 (E3)	15
72483380721505294, 72834674820722635, 72975481296715415, 73891167921933971	IN19A007 (I2), IN17A001 (E1), INXXX466 (E2), 19B (+)	13
72483380721505294, 72834674820722635, 72905112552773752, 72975481296715415, 73468887542677672	IN19A007 (I2), IN17A001 (E1), INXXX464 (E5), INXXX466 (E2), 12B (–)	13

Supplementary Table 3: Converged minimal circuits for DNg100 pruning screen in FANC. All distinct sets of interneurons that appeared at least 10 times out of 1024 pruning screens.

bodyIds	types	count
10242, 10707, 11751, 12021, 162543	IN19A007 (I2), IN17A001 (E1), INXXX466 (E2), IN03A006 (E4), INXXX464 (E5)	465
10715, 11751, 12021, 13905, 162543	IN19B012 (E3), INXXX466 (E2), IN03A006 (E4), IN16B036 (I1), INXXX464 (E5)	129
10707, 11751, 12021, 13905, 17664, 162543	IN17A001 (E1), INXXX466 (E2), IN03A006 (E4), IN16B036 (I1), MNfl10 (–), INXXX464 (E5)	26
10707, 11751, 12021, 13905, 162539, 162543	IN17A001 (E1), INXXX466 (E2), IN03A006 (E4), IN16B036 (I1), IN13A001 (–), INXXX464 (E5)	21
10707, 11751, 12021, 13905, 162543	IN17A001 (E1), INXXX466 (E2), IN03A006 (E4), IN16B036 (I1), INXXX464 (E5)	12
10242, 10707, 11751, 21162, 162543	IN19A007 (I2), IN17A001 (E1), INXXX466 (E2), IN20A.22A036 (+), INXXX464 (E5)	12
10242, 10707, 11751, 12021, 21162, 162543	IN19A007 (I2), IN17A001 (E1), INXXX466 (E2), IN03A006 (E4), IN20A.22A036 (+), INXXX464 (E5)	10

Supplementary Table 4: Converged minimal circuits for DNb08 pruning screen in MANC. All distinct sets of interneurons that appeared at least 10 times out of 1024 pruning screens.

pre. bodyId	post. bodyId	pre. type	pre. nickname	post. type	post. nickname	neuro-transmitter	num. of synapses
10093	10707	DNg100	BDN2	IN17A001	E1	acetylcholine	187
10097	11751	DNxl080		INXXX466	E2	gaba	173
10532	10707	DNg74	web	IN17A001	E1	gaba	160
10086	11751	DNg105		INXXX466	E2	gaba	126
10941	11751	DNxl130		INXXX466	E2	acetylcholine	93
10279	10707	DNxl049		IN17A001	E1	acetylcholine	92
23461	10707	DNfl031		IN17A001	E1	acetylcholine	86
27936	13905	DNfl023		IN16B036	I1	acetylcholine	82
10107	11751	DNg74	web	INXXX466	E2	gaba	80
10291	10707	DNxl134		IN17A001	E1	acetylcholine	75
19287	10707	DNfl036		IN17A001	E1	acetylcholine	73
27523	10707	DNfl025		IN17A001	E1	acetylcholine	73
10420	10707	DNg93		IN17A001	E1	gaba	72
22875	13905	DNg12		IN16B036	I1	acetylcholine	68
10058	11751	DNg108		INXXX466	E2	gaba	62
15249	10707	DNg17		IN17A001	E1	acetylcholine	60
156265	10707	DNfl014		IN17A001	E1	acetylcholine	54
10291	11751	DNxl134		INXXX466	E2	acetylcholine	40
21235	10707	DNfl032		IN17A001	E1	gaba	39
32742	10707	DNg12		IN17A001	E1	acetylcholine	38
32815	10707	DNg12		IN17A001	E1	acetylcholine	37
11220	10707	DNxl127		IN17A001	E1	gaba	36
20782	10707	DNfl034		IN17A001	E1	acetylcholine	34
24753	10707	DNg62	aDN1	IN17A001	E1	acetylcholine	34
31078	10707	DNg12		IN17A001	E1	acetylcholine	33
10656	10707	DNg97	oDN1	IN17A001	E1	acetylcholine	32
21320	13905	DNfl033		IN16B036	I1	acetylcholine	22
14903	10707	DNg17		IN17A001	E1	acetylcholine	21
10107	13905	DNg74		IN16B036	I1	gaba	20
10107	10707	DNg74		IN17A001	E1	gaba	19
27350	10707	DNxl070		IN17A001	E1	gaba	19
14836	13905	DNxl099		IN16B036	I1	acetylcholine	19
27516	10707	DNxn143		IN17A001	E1	acetylcholine	18
10058	10707	DNg108		IN17A001	E1	gaba	17
10532	11751	DNg74		INXXX466	E2	gaba	16
31635	10707	DNg12		IN17A001	E1	acetylcholine	16
13845	13905	DNg44		IN16B036	I1	glutamate	15
28478	10707	DNg12		IN17A001	E1	acetylcholine	15
13257	10707	DNxl103		IN17A001	E1	acetylcholine	15
19287	13905	DNfl036		IN16B036	I1	acetylcholine	15
23953	10707	DNfl030		IN17A001	E1	acetylcholine	14
11354	10707	DNg75		IN17A001	E1	acetylcholine	13
13257	13905	DNxl103		IN16B036	I1	acetylcholine	12
25879	10707	DNfl029		IN17A001	E1	acetylcholine	12
27217	10707	DNfl024		IN17A001	E1	acetylcholine	12
10760	10707	DNa01		IN17A001	E1	acetylcholine	12
10410	11751	DNd03		INXXX466	E2	glutamate	12
11270	11751	DNxl129		INXXX466	E2	acetylcholine	11
21320	10707	DNfl033		IN17A001	E1	acetylcholine	11
17547	10707	DNfl040		IN17A001	E1	acetylcholine	11
17400	10707	DNfl040		IN17A001	E1	acetylcholine	11
10410	10707	DNd03		IN17A001	E1	glutamate	11
11961	13905	DNxl126		IN16B036	I1	gaba	10
16369	10707	DNfl015		IN17A001	E1	acetylcholine	10

Supplementary Table 5: Top descending inputs to DNg100 core CPG circuit interneurons. Table of all descending neurons that make ≥10 synaptic connections onto left front leg E1, E2, and I1 neurons.

bodyId	type	mean motor rhythmicity score
10118	DNa02	0.000000
10126	DNa02	0.015600
14680	DNb08	0.801999
13892	DNb08	0.839170
14966	DNb08	0.841571
14061	DNb08	0.955253
10093	DNg100	0.978602
10339	DNg100	0.983424
29706	DNg12	0.000000
27728	DNg12	0.000000
34253	DNg12	0.000000
30271	DNg12	0.000000
28478	DNg12	0.000000
22875	DNg12	0.000000
24858	DNg12	0.000000
31635	DNg12	0.001649
32424	DNg12	0.014636
31742	DNg12	0.021896
31361	DNg12	0.035059
40338	DNg12	0.093108
31613	DNg12	0.137115
31078	DNg12	0.184643
34862	DNg12	0.219746
35413	DNg12	0.247020
35473	DNg12	0.424952
38587	DNg12	0.647725
32742	DNg12	0.668965
32815	DNg12	0.813234
30919	DNg12	0.905598
22870	DNg12	NaN
26725	DNg12	NaN
29120	DNg12	NaN
30346	DNg12	NaN
30999	DNg12	NaN
31123	DNg12	NaN
32667	DNg12	NaN
33586	DNg12	NaN
34382	DNg12	NaN
24753	DNg62	0.009698
152849	DNg62	0.012459
10656	DNg97	0.040061
11070	DNg97	0.257257
12955	DNp09	0.000000
12926	DNp09	0.000000
14523	MDN	0.000000
13438	MDN	0.000000
13809	MDN	0.321310
14419	MDN	0.429656

Supplementary Table 6: Mean motor rhythmicity scores of selected known motor-related descending neurons in activation screen. DNg97 is the standard cell type of oDN1 [47]. DNg62 is the standard cell type of aDN1 [55].